

Quantitative phase-field modeling of dendritic growth in two and three dimensions

Alain Karma and Wouter-Jan Rappel

*Department of Physics and Center for Interdisciplinary Research on Complex Systems, Northeastern University,
Boston, Massachusetts 02115*

(Received 10 June 1997)

We report the results of quantitative phase-field simulations of the dendritic crystallization of a pure melt in two and three dimensions. These simulations exploit a recently developed thin-interface limit of the phase-field model [A. Karma and W.-J. Rappel, *Phys. Rev. E* **53**, R3017 (1996)], which is given here a detailed exposition. This limit makes it possible to perform efficient computations with a smaller ratio of capillary length to interface thickness and with an arbitrary interface kinetic coefficient. Simulations in one and two dimensions are first carried out to test the accuracy of phase-field computations performed within this limit. Dendrite tip velocities and tip shapes are found to be in excellent quantitative agreement with exact numerical benchmarks of solvability theory obtained by a boundary integral method, both with and without interface kinetics. Simulations in three dimensions exploit, in addition to the asymptotics, a methodology to calculate grid corrections due to the surface tension and kinetic anisotropies. They are used to test basic aspects of dendritic growth theory that pertain to the selection of the operating state of the tip and to the three-dimensional morphology of needle crystals without sidebranches. For small crystalline anisotropy, simulated values of σ^* are slightly larger than solvability theory predictions computed by the boundary integral method assuming an axisymmetric shape, and agree relatively well with experiments for succinonitrile given the uncertainty in the measured anisotropy. In contrast, for large anisotropy, simulated σ^* values are significantly larger than the predicted values. This disagreement, however, does not signal a breakdown of solvability theory. It is consistent with the finding that the amplitude of the $\cos 4\phi$ mode, which measures the departure of the tip morphology from a shape of revolution, increases with anisotropy. This departure can therefore influence the tip selection in a way that is not accurately captured by the axisymmetric approximation for large anisotropy. Finally, the tail shape at a distance behind the tip that is large compared to the diffusion length is described by a linear law $r \sim z$ with a slope dr/dz that is nearly equal to the ratio of the two-dimensional and three-dimensional steady-state tip velocities. Furthermore, the evolution of the cross section of a three-dimensional needle crystal with increasing distance behind the tip is nearly identical to the evolution of a two-dimensional growth shape in time, in accord with the current theory of the three-dimensional needle crystal shape. [S1063-651X(98)09201-0]

PACS number(s): 68.70.+w

I. INTRODUCTION AND SUMMARY

The phase-field approach is rapidly emerging as a method of choice for simulating interfacial pattern formation phenomena in solidification and other systems [1–23]. The widely recognized appeal of this approach is to avoid the explicit tracking of macroscopically sharp phase boundaries. This makes it better suited than more conventional front-tracking methods [24–27] to simulate time-dependent free-boundary problems in three dimensions (3D) or when complex geometries are involved. Tracking is avoided by introducing an order parameter, or phase field ψ , which varies smoothly from one value in the liquid to another value in the solid across a spatially diffuse interface region of thickness W . This field naturally distinguishes the solid and liquid phases and converts the problem of simulating the advance of a sharp boundary to that of solving a stiff system of partial differential equations that govern the evolution of the phase and diffusion fields.

The phase-field method is rooted in continuum models of phase transitions that have appeared in the literature in various contexts [28–30]. However, the introduction of the method—specifically as a computational tool to model solidification—can be traced back to an unpublished derivation by Langer [31], who recast model C of Halperin, Ho-

enberg, and Ma [30] of dynamic critical phenomena into a model describing the crystallization of a pure melt. This model was implemented numerically by Fix [2]. Langer's derivation was published later [1]. Collins and Levine [3] have also written down independently similar phase-field equations and analyzed one-dimensional steady states. Since then, the original model has been modified and reformulated by various authors to address issues of thermodynamic self-consistency [4,5] and have been substantially extended to model the solidification of binary [6–8] and eutectic [9–11] alloys. In addition, more extensive simulations have been carried out. Much of the numerical work to date has focused on the dendritic solidification of a pure melt [12–23] that provides a nontrivial computational test case for the phase-field method. The basic equations for this case are described in Sec. II. In the simplest situation where the surface energy is isotropic, they take the simple form

$$\tau \partial_t \psi = W^2 \nabla^2 \psi - \frac{\partial F(\psi, \lambda u)}{\partial \psi}, \quad (1)$$

$$\partial_t u = D \nabla^2 u + \partial_t h(\psi)/2, \quad (2)$$

where $F(\psi, \lambda u) \equiv f(\psi) + \lambda g(\psi)u$ is a function that has the form of a double-well potential where the relative height of

the two minima is temperature dependent, $h(\psi)$ is a function defined in the next section that describes the generation of latent heat and will be specified below, $u \equiv (T - T_M)/(L/c_p)$ denotes the dimensionless temperature field, W is the interface thickness (on the order of angstroms), τ is the characteristic time of attachment of atoms at the interface ($\sim 10^{-13}$ sec for metallic systems), and λ is a dimensionless parameter that controls the strength of the coupling between the phase and diffusion fields and is typically of order unity. Here T_M is the melting temperature, L is the latent heat of melting, c_p is the specific heat at constant pressure, and D is the thermal diffusivity. It is commonly accepted that these equations only represent a phenomenological description of the underlying microscopic physics of the solid-liquid interface. Therefore they only take on a quantitative meaning in the so-called sharp-interface limit where the phase-field equations reduce to the standard free-boundary problem

$$\partial_t u = D \nabla^2 u, \quad (3)$$

$$V = D(\partial_n u|^- - \partial_n u|^+), \quad (4)$$

$$u_i = -d_0/R - \beta V, \quad (5)$$

where microscopic details of the interface region become unimportant. Here, V is the local normal velocity of the interface, $d_0 = \gamma_0 T_M c_p / L^2$ is the capillary length, R is the principal radius of curvature of the boundary, and β is the kinetic coefficient. In this limit, Langer [1], and then Caginalp [32] using a more formal asymptotic analysis, have derived the expressions

$$d_0 = a_1 \frac{W}{\lambda}, \quad (6)$$

$$\beta \equiv \beta_0 = a_1 \frac{\tau}{\lambda W}, \quad (7)$$

which relate the basic microscopic parameters of the phase-field model to the capillary length d_0 and the kinetic coefficient β , which are both measurable quantities. In these expressions, a_1 is a positive constant of order unity that depends on the details of the assumed form of free energy $F(\psi, \lambda u)$ and is unimportant. These expressions have been extended by Kobayashi [12] and McFadden *et al.* [18] to incorporate crystalline anisotropy, and have provided so far the theoretical basis to relate phase-field computations to the free-boundary problem. Note that Eqs. (6) and (7) have a simple dimensional interpretation. The Gibbs-Thomson condition implies that d_0 and β have dimension of length and inverse velocity, respectively. Furthermore, since only the product λu appears in the phase-field equations, u_i must scale inversely proportionally with λ . It then follows that d_0 and β must scale dimensionally as W/λ and $\tau/W\lambda$, respectively. Also, Eqs. (6) and (7) imply that d_0 and β only fix the ratio W/λ and $\tau/W\lambda$, respectively, but not W and τ independently. Hence, convergence of phase-field computations can only be achieved by decreasing $W \sim \lambda$ and $\tau \sim \lambda^2$ until the results become independent of interface thickness; that is, decreasing W , τ , and λ while keeping d_0 and β fixed as defined by Eqs. (6) and (7).

The first large scale phase-field simulations of Kobayashi [13] produced dendritic structures that resemble qualitatively those seen in experiment. More recent computations by Wheeler *et al.* [14] and Wang and Sekerka [17] have focused on testing quantitatively the convergence of the phase-field method. These studies have highlighted a serious limitation of the phase-field approach. Namely, in practice W , and hence the grid spacing Δx that scales proportionally to W , needs to be chosen quite small compared to the scale of the dendrite pattern to converge to a reliable quantitative solution of the sharp-interface equations. For this reason, computations to date, which can be considered to be reasonably independent of computational parameters, have been restricted to a regime of dimensionless undercooling $\Delta \equiv (T_M - T_\infty)/(L/c_p)$ of order unity [17], where T_∞ is the initial temperature of the melt. In this regime, the interfacial undercooling u_i is dominated by interface kinetics (i.e., $\beta V \gg d_0/R$). Simulations at smaller undercooling seem to exhibit a dependence on interface thickness [14]. For this reason, adaptive meshing [33–35] is actively being pursued to try to overcome the stiffness associated with the diffuse interface region.

This stringent computational limitation of the phase field can be understood [19] to result from the combination of the constraint on the ratio W/d_0 imposed by the assumptions made in deriving Eqs. (6) and (7), and the fact that the computation time to simulate a dendrite structure diverges as $(W/d_0)^{-(2+d)}$ in d dimensions. The constraint on W/d_0 comes from the fact that Eqs. (6) and (7) are only strictly valid in the asymptotic limit of vanishing interface thickness. Mathematically, this limit corresponds to letting $\lambda \rightarrow 0$ [32] with $W = \lambda d_0/a_1$ and $\tau = \lambda^2 \beta d_0/a_1^2$. Thus, in this limit, u is constant across the spatially diffuse interface region, since $W \rightarrow 0$ with respect to the macroscale of the diffusion field. On purely dimensional grounds, the magnitude of the variation of u across the interface scales as $\delta u \sim WV/D$, since u varies locally on a scale $\sim D/V$ in the direction normal to the interface, where V is the local normal velocity of the interface. Therefore neglecting this variation is equivalent to assuming that $\delta u \ll |u_i|$, or $WV/D \ll \beta V$, which is easily seen to yield the constraint

$$\frac{W}{d_0} \ll \frac{D\tau}{W^2} \quad (8)$$

using Eqs. (6) and (7). The scaling of the computation time, in turn, comes from the fact that the number of floating point operations, N_{FP} , necessary to simulate a dendrite is approximately the product of the total number of grid points, which scales as $(\ell/W)^d$, where $\ell = D/V_{\text{tip}}$ is the diffusion length and V_{tip} is the tip velocity, and the number of sweeps through the lattice necessary for the tip to reach a steady-state velocity, which scales as $\ell^2/(D\tau)$ since the time step $\Delta t \sim \tau$. Using the fact $D/V_{\text{tip}} \sim d_0/(D\sigma^*P^2)$ to estimate ℓ , we obtain

$$N_{\text{FP}} \sim \left[\frac{W^2}{D\tau} \right] [\sigma^*P^2]^{-(2+d)} \left[\frac{W}{d_0} \right]^{-(2+d)}, \quad (9)$$

where $P \equiv \rho_{\text{tip}} V_{\text{tip}} / 2D$ is the tip Péclet number, and $\sigma^* \equiv 2Dd_0/\rho_{\text{tip}}^2 V_{\text{tip}}$ is the classic parameter characterizing the

operating state of the dendrite tip. The first term in square brackets on the left-hand side of Eq. (9), which also appears in Eq. (8), is constrained by numerical stability to be of order unity if an explicit scheme is used to time step the diffusion field. It can be made somewhat smaller if an implicit scheme is used instead. The second reflects the increase of the diffusion length with decreasing Δ and P , or decreasing anisotropy and σ^* . Finally, the last factor reflects the very rapid increase in N_{FP} with decreasing interface thickness. Furthermore, the Péclet number scales as $P \approx \Delta^2/\pi$ in 2D and $P \approx -\Delta/\ln(\Delta)$ in 3D for $\Delta \ll 1$. These relations, combined with the estimate of Eq. (9) and the constraint of Eq. (8), show that quantitative computations at small Δ are extremely costly, and not really feasible with current supercomputing technology.

Recently, we have found that this limitation of the phase-field approach can be circumvented to a large degree by rethinking the way in which we analyze the sharp-interface limit of the phase-field equations [19–21]. This was done by deriving a “thin-interface” limit of these equations [19,20], which is physically more realistic in that it assumes that the interface thickness is small compared to the mesoscale of the diffusion field, but remains finite. This is in contrast to the standard asymptotics leading to Eqs. (6) and (7), which assumes that $W \rightarrow 0$ as emphasized above. A similar type of finite W limit has been independently examined by Fife and Penrose [36], albeit not for computational purposes. An analysis of this thin-interface limit, which is a more detailed version of our earlier derivation in [19], is given in Sec. III for both isotropic and anisotropic interfaces. An alternate derivation, based on a higher-order analysis with λ as small parameter, is given in Appendix A for completeness. These analyses yield the same expression for d_0 as Eq. (6), but a modified expression for the kinetic coefficient given by [19]

$$\beta = a_1 \left[\frac{\tau}{\lambda W} - a_2 \frac{W}{D} \right], \quad (10)$$

where the second term on the right-hand side of Eq. (10) originates from including the variation of u across the interface, and a_2 is a positive constant of order unity that depends on the details of the functional forms chosen for $f(\psi)$, $g(\psi)$, and $h(\psi)$. As seen earlier, this variation scales as $\delta u \sim WV/D$, and therefore generates a correction to β that scales as $\sim W/D$. This thin-interface limit has two obvious computational advantages. First, it is not subject to the constraint of Eq. (8) which is only present if one requires that $W/D \ll \beta_0$ in Eq. (10). Therefore it makes it possible to perform simulations with a larger W/d_0 ratio, which reduces dramatically the computation time according to Eq. (9). One main consequence of this reduction is to render simulations at smaller Δ more directly accessible in 2D [19] and to make quantitative 3D simulations [21] possible. Second, the kinetic coefficient can be made to vanish by choosing $\lambda = \lambda^* = \tau D/W^2 a_2$. Thus it makes it possible to simulate the case of negligible interface kinetics that is physically relevant at low undercooling for a large class of materials, especially metallic systems with fast kinetics.

A couple of additional points concerning this limit are worth emphasizing. First, one would have naively expected

that taking into account the variation of u in the interface region would generate corrections to the Gibbs-Thomson condition that are proportional to the normal gradient of u at the boundary ($\partial_n u|^\pm$). While such corrections are indeed generally present in this limit, they turn out to vanish somewhat miraculously if both $f(\psi)$ is chosen to be an even function of ψ , which implies that the stationary profile $\psi_0(x)$ that describes the planar interface at the melting temperature is odd in x about the origin, and $h(\psi)$ and $g(\psi)$ in Eqs. (1) and (2) are chosen to be odd functions of ψ . It is precisely the fact that these corrections can be made to vanish for these special symmetries that renders this limit computationally useful, i.e., in that it gives back a Gibbs-Thomson condition of the standard form.

Second, there is a subtle physical point concerning the interpretation of β in Eq. (10). This result implies that the kinetic coefficient can become negative when $\tau < \lambda a_2 W^2/D$. This conclusion may appear at first sight thermodynamically inconsistent because the solid-liquid interface cannot solidify with $u_i > 0$, which corresponds to an interface temperature larger than T_M . There is, however, no inconsistency. In this thin-interface limit, u_i only represents the boundary condition for u on the interface with respect to the macroscopic (outer) scale of the diffusion field. On the microscopic (inner) scale of the interface u varies across the interface region and changes sign as it crosses this region when $\beta < 0$. Therefore the actual value of u at the interface position defined by $\psi = 0$ is not the same as u_i in this limit. In contrast, in the sharp-interface limit, both values of u become identical and β is always constrained to be positive. This point is examined in more detail in Sec. IV where we analyze 1D growth fronts for parameters of the phase field that correspond to both positive and negative β .

The first goal of this paper is to demonstrate that accurate quantitative solutions of the free-boundary problem described by Eqs. (3)–(5) can be obtained by exploiting the thin-interface limit described above. We examine the solidification of a planar interface in Sec. IV, which is the simplest test case where the steady-state velocity of the interface is known analytically. We then present in Sec. V the results of simulations of dendritic growth in 2D with and without interface kinetics. In previous studies [17,33], the convergence of phase-field computations as a function of interface thickness has been checked by verifying that the Gibbs-Thomson condition is verified at the tip. In contrast, here, we test this convergence by comparing the tip velocity and the interface shape to the numerical solution of the steady-state growth equations, which provides a more direct test. These equations are solved independently by the standard boundary integral method implementation of solvability theory [37–40].

We find that we are able to model dendritic growth accurately down to values of Δ around 0.25. A simulation at this undercooling requires about 100 hours to reach a steady-state velocity on a workstation with a single processor with about a 50 Mflops (megaflops) output. Much shorter times are needed for larger Δ and quantitative results can be obtained with about 12 minutes of central processing unit (CPU) time on the same processor at $\Delta = 0.55$.

The second goal of this paper is to present 3D computations that explore several fundamental aspects of steady-state dendritic growth theory. A methodology is developed in Sec.

VI to incorporate quantitatively the effect of the lattice anisotropy. It makes it possible to speed up the computations even further by using a larger grid spacing and to resolve smaller anisotropies. The results of the computations, which have been briefly exposed elsewhere [21,42], are presented in detail in Sec. VII.

Theoretical progress over the last decade has led to the development of solvability theory to determine the operating state of the dendrite tip [43–52]. In 2D, dynamical simulations based on a sharp-interface [27] or a phase-field approach [19,20] give a good quantitative agreement with this theory. In 3D, however, this theory has remained more uncertain. This is due in part to the fact that it has so far remained too difficult to simulate reliably the free-boundary problem of dendritic growth in 3D using a sharp-interface approach. This has prevented convincing demonstration that the global attractor of the growth dynamics is indeed the steady-state needle crystal predicted by solvability theory. In addition, the predictions of this theory have remained themselves approximate in 3D since they are based on assuming that the crystalline anisotropy and the tip shape are axisymmetric (i.e., are independent of the polar angle ϕ in the plane perpendicular to the dendrite growth axis) [49,50]. It has therefore remained unclear to what degree the existing disagreement between theory and experiment [53–57] is due to this approximation.

The present computations largely remove much of the existing doubt about the validity of solvability theory in 3D. They show that the attractor of the growth dynamics is the underlying steady-state needle crystal predicted by this theory, up to quantitative differences in σ^* values that are most likely due to the limitation of the axisymmetric approximation. In particular, we find that phase-field dendrites grow with a slightly higher σ^* value than predicted by the axisymmetric solvability theory for low anisotropy, and a significantly larger σ^* value for large anisotropy where the departure from a shape of revolution becomes more pronounced. They improve the agreement between theory and experiment for succinonitrile (SCN). A poor quantitative agreement, however, is still found for pivalic acid (PVA). This disagreement could potentially be resolved in the future by including kinetic effects that are neglected here both in the 3D phase-field computations and in the 3D implementation of solvability theory. We only demonstrate in Sec. V B that phase-field computations and solvability calculations that both incorporate interface kinetics give essentially identical results in 2D. We therefore expect an equally good agreement in 3D.

With regard to the shape of the needle crystal, the simulation results show that the departure from a shape of revolution is well described by a single $\cos 4\phi$ mode in the tip region. For the smallest anisotropy simulated here ($\epsilon_4 \sim 0.0066$), the amplitude of this mode is of comparable magnitude to the amplitude predicted by the linear solvability theory of Ben Amar and Brenner [51]. One difference, however, is that we find that this amplitude increases with ϵ_4 whereas their theory predicts that it is independent of ϵ_4 . Note that this is not an actual discrepancy since their theory is only strictly valid for asymptotically small values of ϵ_4 that are presumably outside the range of our simulations. This sensitive dependence of the tip morphology on anisotropy

seen in our simulations should be experimentally verifiable by comparing the amplitude of this $\cos 4\phi$ mode for materials with different anisotropies.

In the dendrite tail, the shape of the needle crystal is found to be described by a linear law $r=Bz$ for distances behind the tip larger than the diffusion length D/V . Moreover, the slope B is nearly equal to the ratio of the 2D and 3D dendrite tip velocities in good agreement with the theory of Brenner [52], which is based on assuming that cross sections of 3D steady-state dendrites behave as two-dimensional growth shapes. Actually, our simulations indicate that this assumption, which is strictly only valid for $B \rightarrow 0$, remains remarkably accurate even in a regime where B is of order unity.

II. PHASE-FIELD MODEL

The basic equations of the phase-field model are derivable from a single Lyapunov functional when expressed in the variational form (VF) [1]

$$\tau(\mathbf{n}) \frac{\partial \psi}{\partial t} = - \frac{\delta \mathcal{F}}{\delta \psi}, \quad (11)$$

$$\frac{\partial U}{\partial t} = \frac{D}{b\lambda} \nabla^2 \frac{\delta \mathcal{F}}{\delta U}, \quad (12)$$

where

$$\mathbf{n} \equiv \frac{\vec{\nabla} \psi}{|\vec{\nabla} \psi|}, \quad (13)$$

is the normal direction to the interface, and

$$\mathcal{F} = \int dV \left[\frac{[W(\mathbf{n})]^2}{2} |\vec{\nabla} \psi|^2 + f(\psi) + b\lambda \frac{u^2}{2} \right] \quad (14)$$

is a phenomenological free energy. Anisotropy in the surface energy and in the kinetics is incorporated as in previous models [12,14,17–21] via the functional dependence of $W(\mathbf{n})$ and $\tau(\mathbf{n})$. The independent variables are ψ and the dimensionless enthalpy

$$U(u, \psi) = u - \frac{h(\psi)}{2}. \quad (15)$$

Equations (11) and (12) imply that

$$\frac{d\mathcal{F}}{dt} \leq 0, \quad (16)$$

if there are no fluxes across the boundaries of the volume where \mathcal{F} is defined, i.e., the dynamics drives the system towards a minimum of free energy. To obtain a phase-field model that reduces to the desired free-boundary problem, it is generally sufficient to require that $f(\psi)$ has the shape of a double-well potential. The simplest choice for $f(\psi)$ that has been traditionally used is

$$f(\psi) = - \frac{\psi^2}{2} + \frac{\psi^4}{4}, \quad (17)$$

with minima at $\psi = \pm 1$ corresponding here to the solid ($\psi = +1$) and liquid ($\psi = -1$) phases. In the way the equations have been written here, there is the additional requirement that $h(\psi)$ satisfy the condition

$$\frac{h(+1) - h(-1)}{2} = 1 \quad (18)$$

to ensure that a unit amount of latent heat is produced at the interface with the temperature field normalized by L/c , for $f(\psi)$ defined by Eq. (17). Note that Eqs. (11) and (12) reduce to the form of Eqs. (1) and (2) if $g(\psi)$ and $h(\psi)$ are related by

$$g(\psi) = \frac{b}{2} h(\psi), \quad (19)$$

where b is just a normalization constant that is introduced such that Eq. (18) can always be satisfied for a given choice of function $g(\psi)$. The VF was introduced by Langer in his adaptation of model C of Halperin, Hohenberg, and Ma, for solidification (Eqs. 3.13–3.16 in Ref. [1]). He wrote down Eqs. (11) and (12) specifically for the case where $g(\psi) = \psi$, in which case Eqs. (18) and (19) require that $h(\psi) = \psi$ and $b = 1$. Since then, this formulation has been reinterpreted by Penrose and Fife [4] and Wang *et al.* [5] in terms of an entropy functional \mathcal{S} meant to represent the total entropy of the system in some given volume. In their interpretation, Eq. (16) becomes effectively replaced by the condition of positive entropy production $d\mathcal{S}/dt \geq 0$, if no fluxes are present at the boundaries of the volume. This entropy formulation is equivalent to the VF in that it yields the same phase-field equations [Eqs. (11) and (12) above], and yields the same thermodynamic consistency relation between $g(\psi)$ and $h(\psi)$ as Eq. (19).

It is important to stress that the constraint imposed by Eq. (19) is not necessary to obtain phase-field equations that reduce to the desired free-boundary problem in the limit of a thin interface. The isothermal variational formulation (IVF) defined by the equations

$$\tau(\mathbf{n}) \frac{\partial \psi}{\partial t} = - \frac{\delta \mathcal{F}_{\text{iso}}}{\delta \psi}, \quad (20)$$

$$\partial_t u = D \nabla^2 u + \partial_t h/2, \quad (21)$$

where

$$\mathcal{F}_{\text{iso}} = \int dV \left[\frac{[W(\mathbf{n})]^2}{2} |\vec{\nabla} \psi|^2 + f(\psi) + \lambda g(\psi) u \right], \quad (22)$$

conserves the total enthalpy and has the advantage that it allows one to choose the functions $g(\psi)$ and $h(\psi)$ independently. In this case, the phase-field equations are not derived from a single Lyapounov functional. They are only variational isothermally in the trivial case where u is taken to be constant.

For computational purposes, we have used

$$g(\psi) = \psi - 2\psi^3/3 + \psi^5/5. \quad (23)$$

This form, which has been used previously [5,58], has the advantage that it keeps the minima of free energy at fixed values $\psi = \pm 1$ independent of the value of u . For $h(\psi)$, we have used either the form

$$h_{\text{VF}}(\psi) \equiv 15(\psi - 2\psi^3/3 + \psi^5/5)/8, \quad (24)$$

with $b = 16/15$, which correspond to the VF of the phase-field equations, or the form

$$h_{\text{IVF}}(\psi) \equiv \psi \quad (25)$$

that is to be used in conjunction with the IVF of the equations. Interestingly, as described in Sec. V, the latter form turns out to be computationally more efficient for simulating dendritic growth because results converge faster as a function of the grid spacing Δx . It is therefore used exclusively here for the 3D computations. One point is worth emphasizing. The VF represents a thermodynamically more consistent description of a first-order phase transformation in that both equations can be derived from a single free-energy functional. It is therefore perhaps more appealing than the IVF from a formal standpoint. Both formulations, however, reduce to identical free-boundary problems in the limit that the interface thickness is small. Hence, in our view, the relative advantage of one formulation over the other needs to be evaluated purely on the basis of computational efficiency and accuracy. This is especially true since, as emphasized in the introduction, the phase-field model only takes on a quantitative meaning in the limit where the microscopic details of the interface region are irrelevant, and are only reflected in macroscale parameters such as d_0 and β .

III. ASYMPTOTICS

A. Isotropic interfacial energy and kinetics

For clarity of exposition, it is best to first derive the thin-interface limit in the case where the interfacial energy and kinetics are independent of interface orientation. We then consider how the results become modified when we incorporate anisotropy in the surface energy and kinetics. We first rewrite the phase-field equations in dimensionless form by measuring length in units of ℓ_c and time in units of ℓ_c^2/D , where ℓ_c is taken to be a fixed mesoscopic length scale that sets the scale of the diffusion field and the solidification pattern in a given simulation. All that we need to assume here is that the interface thickness is small compared to the macro scale of the solidification pattern, not that it vanishes. Equations (1) and (2) then become

$$\alpha p^2 \partial_t \psi = p^2 \nabla^2 \psi - f_\psi - \lambda g_\psi u, \quad (26)$$

$$\partial_t u = \nabla^2 u + \partial_t h/2, \quad (27)$$

where we have defined the small parameter $p \equiv W/\ell_c$ and the dimensionless diffusivity $\alpha \equiv D\tau/W^2$. If we interpret V_c and $\ell_c \sim D/V_c$ as the characteristic interface velocity and diffusion length in the problem, respectively, then p is essentially playing the role of an ‘‘interface Péclet number.’’ We now look for solutions of Eqs. (26) and (27) for $p \ll 1$ in an inner region which corresponds to the spatially diffuse interface region where ψ varies rapidly, and an outer region

which corresponds to the bulk phases away from the interface. We expand the inner solutions in powers of p as

$$\psi = \psi_0 + p\psi_1 + p^2\psi_2 + \dots, \quad (28)$$

$$u = u_0 + pu_1 + p^2u_2 + \dots \quad (29)$$

and expand similarly the outer solutions as $\tilde{\psi} = \tilde{\psi}_0 + p\tilde{\psi}_1 + \dots$, and $\tilde{u} = \tilde{u}_0 + p\tilde{u}_1 + \dots$. Since in the outer region $\tilde{\psi}$ is constant in each phase (i.e., $\tilde{\psi} = \pm 1$), \tilde{u}_j simply obeys the diffusion equation

$$\partial_i \tilde{u}_j = \nabla^2 \tilde{u}_j \quad (30)$$

for all orders in an expansion in p . To look for the solutions in the inner region, we start by rewriting the phase-field equations (26) and (27) in terms of a local orthogonal set of curvilinear coordinates (ξ_1, ξ_2, ξ_3) that moves with the instantaneous normal velocity of the interface; ξ_3 measures length along the normal direction, and ξ_1 and ξ_2 measure arclength along the two principal directions of the interface defined by $\psi = 0$. Furthermore, we define the inner variable $\eta = \xi_3/p$ and the dimensionless interface velocity $v = V\ell_c/D$ and curvature $\kappa = \ell_c(1/R_1 + 1/R_2)$, where R_1 and R_2 denote the two principal radii of curvature of the boundary, and V is the instantaneous normal interface velocity. Rewriting Eqs. (26) and (27) in terms of η and the above quantities, we obtain

$$p(\alpha v + \kappa) \partial_\eta \psi + \partial_\eta^2 \psi - f_\psi - \lambda g_\psi \mu = 0, \quad (31)$$

$$p(v + \kappa) \partial_\eta u + \partial_\eta^2 u - pv \partial_\eta h/2 = 0, \quad (32)$$

where we have neglected higher-order terms in p^2 which turn out to be unimportant at the end of the calculation. Substituting Eqs. (28) and (29) into Eqs. (26) and (27), we obtain at leading order

$$\partial_\eta^2 \psi_0 - f_\psi^0 - \lambda g_\psi^0 \mu_0 = 0, \quad (33)$$

$$\partial_\eta^2 \mu_0 = 0, \quad (34)$$

where we have defined $f_\psi^0 \equiv f_\psi(\psi_0)$ and $g_\psi^0 \equiv g_\psi(\psi_0)$. These equations have the trivial solutions, $u_0 = 0$, and

$$\psi_0 = -\tanh(\eta/\sqrt{2}), \quad (35)$$

for $f_\psi^0 = -\psi_0 + \psi_0^3$. At first order in p , we obtain the system of linear equations

$$\mathcal{L}\psi_1 = \lambda g_\psi^0 \mu_1 - (\alpha v + \kappa) \partial_\eta \psi_0, \quad (36)$$

$$\partial_\eta \left[\partial_\eta \mu_1 - \frac{v}{2} h^0 \right] = 0, \quad (37)$$

where we have defined the linear operator

$$\mathcal{L} = \partial_\eta^2 - f_{\psi\psi}^0 \quad (38)$$

and the functions, $f_{\psi\psi}^0 = -1 + 3\psi_0^2$, $g_\psi^0 \equiv g_\psi(\psi_0)$, and $h^0 \equiv h(\psi_0)$. We first note that Eq. (37) can be integrated directly, which yields

$$-\frac{v}{2} h^0 + \partial_\eta \mu_1 = A, \quad (39)$$

where A is a first integration constant. Now integrating once more the above equation yields

$$u_1 = \bar{u}_1 + A\eta + \frac{v}{2} \int_0^\eta d\eta' h^0, \quad (40)$$

where \bar{u}_1 is a second integration constant. The rest of the calculation proceeds in two steps. First, a relation between the two integration constants, \bar{u}_1 and A , is derived using a solvability condition for the existence of a nontrivial solution ψ_1 . Second, A and the boundary conditions for u on the two sides of the boundary are derived by matching the solutions in the inner and outer regions. The first step is carried out by first differentiating Eq. (33) with respect to η , which yields $\mathcal{L}\partial_\eta \psi_0 = 0$. Now, since this equation implies that $\partial_\eta \psi_0$ is a homogeneous solution of Eq. (36), and the linear operator \mathcal{L} is self-adjoint, the right-hand side of Eq. (36) must be orthogonal to $\partial_\eta \psi_0$ for a solution ψ_1 to exist. This yields the solvability condition

$$\int_{-\infty}^{+\infty} \partial_\eta \psi_0 [\lambda g_\psi^0 \mu_1 - (v\alpha + \kappa) \partial_\eta \psi_0] d\eta = 0. \quad (41)$$

Let us now consider the matching conditions. The condition that the slopes of the two solutions match on the solid and liquid side of the interface in the regions defined by $1 \ll |\eta| \ll p^{-1}$ implies that

$$\lim_{\eta \rightarrow \pm\infty} \partial_\eta u_1 = \lim_{\xi_3 \rightarrow 0^\pm} \partial_{\xi_3} \tilde{u}_0 \equiv \partial_{\xi_3} \tilde{u}_0 |^\pm. \quad (42)$$

Applying the above matching condition to Eq. (39) and using the fact that $\lim_{\eta \rightarrow \pm\infty} h^0(\eta) = \mp 1$, we obtain at once that

$$\frac{v}{2} + \partial_{\xi_3} \tilde{u}_0 |^+ = A, \quad (43)$$

$$-\frac{v}{2} + \partial_{\xi_3} \tilde{u}_0 |^- = A. \quad (44)$$

Eliminating A between these two equations we recover at once the usual heat conservation condition

$$v = \partial_{\xi_3} \tilde{u}_0 |^- - \partial_{\xi_3} \tilde{u}_0 |^+. \quad (45)$$

To determine the conditions for the outer solution on the two sides of the interface, we expand \tilde{u} in the matching regions in terms of the outer variable ξ_3 . This yields

$$\tilde{u} = u_i^\pm + \partial_{\xi_3} \tilde{u}_0 |^\pm \xi_3, \quad (46)$$

where we have defined the temperatures on both sides of the solid-liquid interface at order p by $u_i^\pm \equiv \lim_{\xi_3 \rightarrow 0^\pm} p \tilde{u}_1$, and we have used the fact that the interface is isothermal at leading order since $\lim_{\xi_3 \rightarrow 0^\pm} \tilde{u}_0 = u_0 = 0$. In the matching regions on both sides of the interface, the inner solution takes the form

$$u = p \left(\bar{u}_1 + \frac{v}{2} F^\pm \right) + \partial_{\xi_3} \tilde{u}_0 |^\pm \xi_3, \quad (47)$$

where we have used Eqs. (43) and (44) to eliminate A in Eq. (40) for each side (+) and (-) of the interface, respectively, and we have defined the constants

$$F^\pm = \int_0^{\pm\infty} d\eta (h^0 \pm 1). \quad (48)$$

Equating the right-hand side of Eqs. (46) and (47), we obtain the desired relations

$$u_i^\pm = p \left(\bar{u}_1 + \frac{v}{2} F^\pm \right), \quad (49)$$

where the constant \bar{u}_1 is defined by the solvability condition of Eq. (41). Two points are worth emphasizing. First, Eq. (41) implies that u_i^\pm includes a term that is proportional to A and, hence, to the normal gradient of the diffusion field ($\partial_{\xi_3} \tilde{u}$) at the boundary for an arbitrary choice of functions f and g in the phase-field equations. However, it is easy to see that the term proportional to A vanishes identically as long as f and g are even and odd functions of ψ , respectively [i.e., $f(-\psi) = f(\psi)$ and $g(-\psi) = -g(\psi)$]. In this case Eq. (33) implies that both $\partial_\eta \psi_0$ and $g_\psi^0 = g_\psi(\psi^0(\eta))$ are even functions of η , and that

$$\int_{-\infty}^{+\infty} d\eta \partial_\eta \psi_0 g_\psi^0 A \eta = 0. \quad (50)$$

This integral vanishes since the product $\partial_\eta \psi_0 g_\psi^0 \eta$ is odd in η . Secondly, for a general choice of function h , Eq. (48) implies that $F^+ \neq F^-$, and therefore that $u_i^+ \neq u_i^-$. So, in general, there is a temperature discontinuity at the interface on the scale of the outer solution. This discontinuity, however, vanishes if h is chosen in addition to be an odd function of ψ . It is straightforward to see that in this case Eq. (48) implies that

$$F^\pm \equiv F = \int_0^\infty d\eta (h^0 + 1) \quad (51)$$

and therefore that

$$u_i^\pm \equiv u_i = p \left(\bar{u}_1 + \frac{v}{2} F \right). \quad (52)$$

The main conclusion is that the standard form of the velocity-dependent Gibbs-Thomson condition is obtained if both g and h are odd functions of ψ , and f is an even function of ψ , which is in itself rather miraculous. Combining Eqs. (40), (41), and (50), we obtain that

$$\bar{u}_1 = -\frac{I}{\lambda J} (\alpha v + \kappa) + \frac{K}{2J} v, \quad (53)$$

where we have defined the integrals

TABLE I. Numerical values for the solvability integrals and constants for two choices of $h(\psi)$.

| $h(\psi)$ | I | J | K | F | a_1 | a_2 |
|------------------------|---------------|-------|--------|-----------------|--------|--------|
| $h_{\text{IVF}}(\psi)$ | $2\sqrt{2}/3$ | 16/15 | 0.1360 | $\sqrt{2}\ln 2$ | 0.8839 | 0.6267 |
| $h_{\text{VFF}}(\psi)$ | $2\sqrt{2}/3$ | 16/15 | 0.2236 | 0.4941 | 0.8839 | 0.3981 |

$$I = \int_{-\infty}^{+\infty} d\eta (\partial_\eta \psi_0)^2, \quad (54)$$

$$J = - \int_{-\infty}^{+\infty} d\eta \partial_\eta \psi_0 g_\psi^0, \quad (55)$$

$$K = \int_{-\infty}^{+\infty} d\eta \partial_\eta \psi_0 g_\psi^0 \int_0^\eta d\eta' h^0. \quad (56)$$

Substituting this expression for \bar{u}_1 into Eq. (52), we obtain

$$u_i = -\frac{a_1}{\lambda} p \kappa - \frac{a_1 \alpha}{\lambda} \left[1 - a_2 \frac{\lambda}{\alpha} \right] p v, \quad (57)$$

with

$$a_1 = \frac{I}{J}, \quad (58)$$

$$a_2 = \frac{K + JF}{2I}. \quad (59)$$

The values of the solvability integrals I , J , K , and F and the resulting values for the constants a_1 and a_2 are given in Table I for the two choices of $h(\psi)$ used in this paper: $h(\psi) = h_{\text{IVF}}(\psi) = \psi$ and $h(\psi) = h_{\text{VFF}}(\psi) = 15(\psi - 2\psi^3/3 + \psi^5/5)/8$. It is easy to see that Eq. (57) is identical to the standard velocity-dependent Gibbs-Thomson condition

$$u_i = -d_0(1/R_1 + 1/R_2) - \beta v, \quad (60)$$

where d_0 and β are defined by Eqs. (6) and (10), respectively. Finally, Eq. (10) can be rewritten in the form

$$\beta = \beta_0 \left[1 - \lambda \frac{a_2 d_0}{D \beta_0} \right] \quad (61)$$

by expressing W and τ in terms of d_0 and β_0 . In this form, the correction to the kinetic coefficient appears as a higher-order term in an asymptotic expansion in λ similar to the one used by Caginalp and others [18] to analyze the sharp-interface limit of the phase-field model. In this expansion, carried out in Appendix A, the surface tension and kinetic terms in the Gibbs-Thomson condition are $O(1)$ quantities and the above $O(\lambda)$ correction to the leading order kinetic coefficient β_0 is obtained from the solvability condition that there exists an inner phase-field solution at $O(\lambda^2)$, whereas in the present asymptotics the interface is isothermal at leading order and the surface tension and kinetic terms are treated as small $O(p)$ corrections that are both obtained from the solvability condition for the existence of ψ_1 .

B. Anisotropic interfacial energy and kinetics

We now examine the more physically realistic situation where both $W(\mathbf{n})$ and $\tau(\mathbf{n})$ are functions of the normal direction \mathbf{n} . The main result that we obtain is the interface condition

$$u_i = -\frac{a_1}{\lambda} \sum_{i=1,2} [W(\mathbf{n}) + \partial_{\theta_i}^2 W(\mathbf{n})] \frac{1}{R_i} - \beta(\mathbf{n})V, \quad (62)$$

where

$$\beta(\mathbf{n}) = \frac{a_1}{\lambda} \frac{\tau(\mathbf{n})}{W(\mathbf{n})} \left[1 - a_2 \lambda \frac{W(\mathbf{n})^2}{D\tau(\mathbf{n})} \right], \quad (63)$$

and where $\bar{\theta}_1$ and $\bar{\theta}_2$ are the angles between the normal and the local principal directions on the interface. This result can be derived in a relatively simple way. For this purpose, we first note that the expression for the kinetic coefficient can be obtained by considering solely the motion of a planar interface perpendicular to \mathbf{n} . This is equivalent to carrying out the same calculation as for the isotropic case above, but with zero curvature. This implies that the expression for $\beta(\mathbf{n})$ must be identical to Eq. (10) with τ simply replaced by $\tau(\mathbf{n})$ and W replaced by $W(\mathbf{n})$. Similarly, the surface tension term can be derived by considering solely a stationary interface. One way to derive this term is to repeat the asymptotic calculation of Sec. III A above including the extra partial derivatives in the phase-field equations that are generated by taking the functional derivative of the free energy with W replaced by $W(\nabla\psi/|\nabla\psi|)$. This calculation is relatively straightforward to carry out in 2D along the lines of Ref. [18]. It becomes more tedious in 3D because of the lengthy form of the anisotropic phase-field equations, although much of this tediousness is removed by making elegant use as in Wheeler and McFadden [59] of the ξ -vector formalism of Cahn and Hoffman [60] in a phase-field context. Here, we only give a simple physically based derivation, equally valid, which consists of minimizing the total free energy \mathcal{F}_{iso} of the system under isothermal condition. This is directly analogous to the way in which the anisotropic Gibbs-Thomson condition is usually derived in the sharp-interface limit. Let us consider an inclusion of solid in a total volume V of solid and liquid that is taken to be constant. We require that the variation of the total free energy with respect to an infinitesimal perturbation of the interface of arbitrary shape vanishes, or that

$$\delta(\mathcal{F}_{\text{iso}} - \mathcal{F}_0) = 0, \quad (64)$$

where \mathcal{F}_0 is some arbitrary constant. The separate contributions of the bulk and surface energy terms can be made explicit by choosing $\mathcal{F}_0 = [f_B + \lambda g(-1)u]V$, with $f_B \equiv f(\pm 1) = -1/4$. With this choice, \mathcal{F}_0 is just a constant that corresponds to the total free energy of the system with the volume V occupied solely by the liquid phase. Combining the expression for \mathcal{F}_{iso} given by Eq. (22) and the expression for \mathcal{F}_0 above, Eq. (64) becomes

$$\delta \left\{ \int_V dV [W(\mathbf{n})^2/2 + |\nabla\psi|^2 + f(\psi) - f_B] + \lambda u \int_V dV [g(\psi) - g(-1)] \right\} = 0, \quad (65)$$

where the first and second integrals are over the fixed volume V and represent the surface and bulk energy contributions, respectively. Note that the integrand of the first integral term in the equation above vanishes everywhere except in the region near the interface, whereas the integrand of the second integral term is a constant that is equal to $g(+1) - g(-1) = J$ [with J defined by Eq. (55)] everywhere in the solid phase and that vanishes in the liquid phase. Therefore in the limit where the interface width is small compared to the size of the solid inclusion, we can rewrite Eq. (65) in the form

$$\delta \left(\int_{S_1} dS \gamma(\mathbf{n}) + \lambda J u \int_{V_1} dV \right) = 0, \quad (66)$$

where S_1 is the surface bounding the solid inclusion of volume V_1 and where the surface energy

$$\gamma(\mathbf{n}) \equiv W(\mathbf{n}) \int_{-\infty}^{+\infty} d\eta [(\partial_\eta \psi_0)^2/2 + f(\psi_0) - f_B] = W(\mathbf{n})I. \quad (67)$$

As before, ψ_0 denotes the stationary one-dimensional phase-field profile given by Eq. (33), where $\eta = \xi_3/W$ is the local coordinate along the normal, and the constant I is defined by Eq. (54). The second equality on the right-hand side of Eq. (67) can be obtained simply by multiplying the right-hand side of Eq. (33) by $\partial_\eta \psi_0$, and integrating over η , which yields

$$\frac{(\partial_\eta \psi_0)^2}{2} - [f(\psi_0) - f_B] = C, \quad (68)$$

where C is a constant of integration. Since $f(\psi_0) - f_B = 0$ in the bulk phases, this constant must vanish. Therefore the integral on the right-hand side of Eq. (67) is exactly equal to the constant I defined by Eq. (54). Finally, the variation of Eq. (66) is well known and yields at once the curvature-dependent part of the Gibbs-Thomson condition defined in Eq. (62).

IV. ONE-DIMENSIONAL STEADY STATES

A. Sharp-interface steady states

In order to illustrate the practical implementation of the thin-interface limit developed in the preceding sections, it is useful to first consider the steady-state growth of a planar interface for undercooling $\Delta > 1$ [61]. This problem has the advantage that it is exactly soluble analytically in the sharp-interface limit and that it is relatively simple to investigate computationally since it is only one dimensional. The sharp-interface equations that describe this problem consist of the diffusion equation expressed in a frame moving at constant velocity V with the interface in the $+x$ direction,

$$V\partial_x u + D\partial_x^2 u = 0, \quad (69)$$

together with the interface boundary conditions

$$V = -D\partial_x u, \quad (70)$$

$$u_i = -\beta V, \quad (71)$$

and the far-field boundary condition

$$u(+\infty) = -\Delta. \quad (72)$$

It is easy to verify that Eqs. (69)–(72) have an exact solution given by

$$V = \frac{\Delta - 1}{\beta}, \quad (73)$$

with the temperature profile

$$u = \exp\left[-\frac{V}{D}x\right] - \Delta \quad (74)$$

in the liquid ($x \geq 0$), and $u = 1 - \Delta$ in the solid ($x \leq 0$).

B. Phase-field steady states

In order to relate the sharp-interface and phase-field formulations we need to calculate the analog of Eq. (73) for the steady states of the phase-field model. In 1D, the phase-field equations take the form

$$\tau\partial_t\psi = W^2\partial_x^2\psi + [\psi - \lambda u(1 - \psi^2)][1 - \psi^2], \quad (75)$$

$$\partial_t u = D\partial_x^2 u + \partial_t\psi/2, \quad (76)$$

where we restrict for simplicity our attention to the case $h(\psi) = h_{\text{VF}}(\psi) = \psi$. The VF gives qualitatively identical results. The steady-state growth equations are simply obtained by rewriting Eqs. (75) and (76) in the moving frame of the interface, which yields

$$\tau V\partial_x\psi + W^2\partial_x^2\psi + [\psi - \lambda u(1 - \psi^2)][1 - \psi^2] = 0, \quad (77)$$

$$V\partial_x u + D\partial_x^2 u - V\partial_x\psi/2 = 0. \quad (78)$$

The solution of these equations with u subject to the far-field boundary condition Eq. (72) determines the planar interface velocity as a function of the undercooling.

This nonlinear boundary value problem was solved numerically using a Newton-Raphson iteration scheme. For this purpose, Eqs. (77) and (78) were discretized with N equally spaced mesh points inside the interval $x \in [-d, d]$ with the interface ($\psi = 0$) fixed at $x = 0$. The spatial derivatives were represented using fourth-order accurate [i.e., $O(\Delta x^4)$] finite difference formulas for accuracy. The unknown values of ψ and u at the mesh points, and V , were then determined using a Newton-Raphson solver with the appropriate boundary conditions at the two end points of the interval. One technical point should be mentioned. The problem was not solved by imposing the far-field boundary condition Eq. (72) directly. This would require, in principle, choosing $d \gg l$, where $l = D/V$ is the diffusion length, and hence unreason-

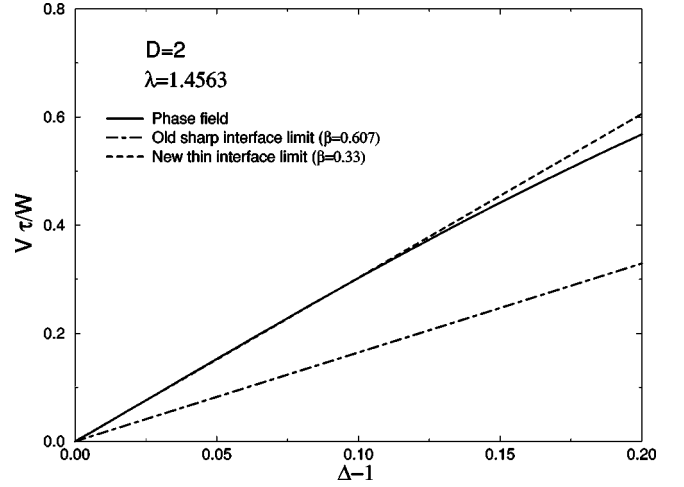


FIG. 1. Numerically calculated values of $V\tau/W$ vs $\Delta - 1$ for the planar steady states of the phase-field model compared to the exact prediction of Eq. (73) with β predicted by the sharp-interface limit [Eq. (7)] and by the thin-interface limit [Eq. (10)].

ably large values of N at small velocity. This difficulty was circumvented by noting that ψ and u are only nontrivial unknowns in the interfacial region where ψ varies rapidly. Outside this region ψ and u have trivial solutions, i.e., $\psi = \pm 1$, $u = 1 - \Delta$ in the solid, and u is a decaying exponential in the liquid. Therefore Eqs. (77) and (78) were solved over a fixed interval by choosing d to be much larger than W but independent of velocity. Boundary conditions on ψ and u were applied at $x = \pm d$ that match to these trivial solutions. This method allowed us to calculate steady states for arbitrarily small V with $d \ll l$. The choices $d = 20$, $N = 100$, and $\Delta x/W = 0.4$ with $W = \tau = 1$ were found to yield interface velocities accurate to less than one-tenth of a percent. Numerically calculated values of V vs $\Delta - 1$ are shown in Fig. 1. Steady-state interface and diffusion profiles are illustrated in Fig. 2. These results were checked by integrating the dynamical equations (75) and (76) for a few values of Δ . These simulations showed that after some dynamical transient the interface reached the velocity and stationary profiles predicted by the numerical solution of the steady-state problem.

C. Comparison of sharp-interface and phase-field steady states

The sharp-interface and phase-field steady states can be compared by expressing β in Eq. (73) in terms of the param-

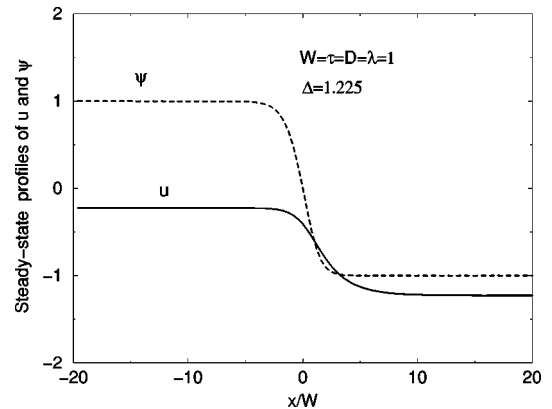


FIG. 2. Calculated steady-state profiles of u and ψ for $\Delta = 1.225$.

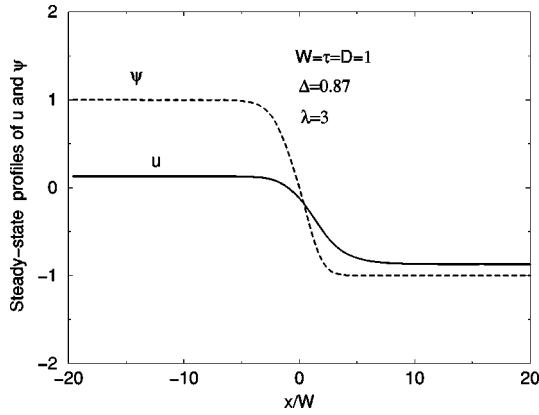


FIG. 3. Example of calculated 1D steady-state profiles of u and ψ for a case where the kinetic coefficient β predicted by the thin-interface limit [Eq. (10)] is negative. Steady-state solutions are dynamically unstable for $\beta < 0$, both in the sharp-interface theory and in the phase-field model, and are therefore not physically relevant.

eters τ , W , λ , and D of the phase-field model. This can be done either by using the expression for β predicted by the standard sharp-interface limit [Eq. (7)] or by the thin-interface limit [Eq. (10)]. Both sets of comparisons are made in Fig. 1 in order to contrast the relative computational advantage of these two asymptotic limits. The results of this figure can be understood by noting that Eq. (73) can be rewritten in the form

$$p \equiv \frac{WV}{D} = \frac{\lambda}{\alpha a_1} \left[\frac{\Delta - 1}{1 - a_2 \lambda / \alpha} \right], \quad (79)$$

by using Eq. (10) to eliminate β . This implies that $p \rightarrow 0$ as $\Delta \rightarrow 1$, and therefore that the thin-interface limit should give an exact agreement with Eq. (73) as $\Delta \rightarrow 1$, which is what is seen in Fig. 1. In contrast, the standard sharp-interface limit does not predict β correctly unless the additional constraint $\lambda/\alpha \ll 1$ is satisfied. Since λ/α is of $O(1)$ in the present example, this limit remains inaccurate even though the diffusion length becomes much larger than W as $\Delta - 1 \rightarrow 0$! The computational advantage of the thin-interface limit is seen here to depend solely on the fact that it predicts a kinetic coefficient that remains valid for a thicker interface.

D. The case of negative kinetic coefficient ($\beta < 0$)

We conclude this section by examining the case where the kinetic coefficient predicted by the thin-interface limit becomes negative. This occurs according to Eq. (10) when $a_2 \lambda W^2 / D \tau > 1$. To see what to expect in this case, let us first consider the prediction of the sharp-interface theory. It predicts that for $\beta < 0$ there should exist a steady-state planar solidification front for $\Delta < 1$ with a velocity given by Eq. (73). However, an analysis of sharp-interface equations reveals that planar steady states are linearly unstable for $\beta < 0$, and are therefore not physically relevant. In this case, the interface slows down as $V \sim t^{-1/2}$, in the same way as for $\beta \geq 0$ since the kinetics become irrelevant when $V \rightarrow 0$. The same is true in phase-field simulations. Solutions of Eqs. (77) and (78) exist for $\beta < 0$ and $\Delta < 1$ as illustrated in Fig. 3. We verified that these solutions are unstable by feeding the steady-state profiles of u and ψ , computed by solving Eqs.

(77) and (78), as inputs into the 1D time-dependent code that integrates Eqs. (75) and (76). The interface evolved into a dynamical state with a velocity that decreases slowly as $\sim t^{-1/2}$ and is the same dynamical attractor as for $\beta > 0$.

V. TWO-DIMENSIONAL SIMULATIONS

In this section we describe our phase-field results for dendritic growth in 2D. We consider growth without and with kinetics successively.

A. Without kinetics

In 2D, the Gibbs-Thomson condition defined by Eq. (62) becomes simply

$$u_i = -d_0(\mathbf{n})/R - \beta(\mathbf{n})V, \quad (80)$$

where

$$d_0(\mathbf{n}) = \frac{a_1}{\lambda} [W(\mathbf{n}) + \partial_{\bar{\theta}}^2 W(\mathbf{n})] \quad (81)$$

and $\bar{\theta}$ is the angle between the normal to the interface and some fixed crystalline axis (e.g., z axis). We choose here a standard fourfold anisotropy defined by

$$d_0(\mathbf{n}) = d_0 [a_s(\mathbf{n}) + \partial_{\bar{\theta}}^2 a_s(\mathbf{n})] \quad (82)$$

and

$$a_s(\mathbf{n}) = \bar{a}_s [1 + \epsilon' (n_x^4 + n_y^4)] = \bar{a}_s [1 + \epsilon' (\sin^4 \bar{\theta} + \cos^4 \bar{\theta})]. \quad (83)$$

The anisotropy strength is characterized by the parameter ϵ_4 that can be measured experimentally by examining the deviation of an equilibrium shape from a circle. For small ϵ_4 , this deviation is given by

$$R(\theta) = R_0 [1 + \epsilon_4 \cos 4\bar{\theta}], \quad (84)$$

where R is the radial polar coordinate measured from a fixed origin.

In this paper we will use ϵ_4 as the measure of the anisotropy and it is easy to check that \bar{a}_s and ϵ' are related to ϵ_4 by the expressions

$$\bar{a}_s = (1 - 3\epsilon_4), \quad (85)$$

$$\epsilon' = \frac{4\epsilon_4}{1 - 3\epsilon_4}. \quad (86)$$

The 2D phase-field equations are obtained by replacing W by $W(\mathbf{n})$ in the gradient term of the free energy, which yields after functional differentiation

$$\partial_t u = D \nabla^2 u + \frac{1}{2} \partial_t h(\psi), \quad (87)$$

$$\begin{aligned}
\tau(\mathbf{n})\partial_t\psi &= [\psi - \lambda u(1 - \psi^2)](1 - \psi^2) + \vec{\nabla} \cdot [W(\mathbf{n})^2 \vec{\nabla} \psi] \\
&+ \partial_x \left(|\vec{\nabla} \psi|^2 W(\mathbf{n}) \frac{\partial W(\mathbf{n})}{\partial(\partial_x \psi)} \right) \\
&+ \partial_y \left(|\vec{\nabla} \psi|^2 W(\mathbf{n}) \frac{\partial W(\mathbf{n})}{\partial(\partial_y \psi)} \right). \quad (88)
\end{aligned}$$

The interface width W depends on the orientation of the interface and is given by

$$\begin{aligned}
W(\mathbf{n}) &= W_0 a_s(\mathbf{n}) \\
&= W_0(1 - 3\epsilon_4) \left[1 + \frac{4\epsilon_4}{1 - 3\epsilon_4} \frac{(\partial_x \psi)^4 + (\partial_y \psi)^4}{|\vec{\nabla} \psi|^4} \right]. \quad (89)
\end{aligned}$$

We first focus our attention on growth in the limit of vanishing interface kinetics. This limit is obtained by setting $\tau(\mathbf{n})$ and λ equal to the values

$$\tau^*(\mathbf{n}) = \tau_0 a_s(\mathbf{n})^2, \quad (90)$$

$$\lambda^* = \frac{1}{a_2} \frac{D\tau_0}{W_0^2} \quad (91)$$

that make the kinetic coefficient β defined by Eq. (63) vanish identically. Equations (87) and (88) were discretized using standard second-order finite difference formulas, except $\nabla^2 \psi$ which was discretized using a nine-point formula with nearest and next nearest neighbors which reduces the grid anisotropy. The ψ and u fields were time stepped using, respectively, a first-order Euler scheme and a second-order implicit Crank-Nicholson scheme [62]. For smaller values of D , we also used a second version of the code where u is time stepped with an Euler scheme. The simulations were performed on two-dimensional lattices of rectangular sizes $N_x \times N_y$ and constant grid spacing Δx in both directions. Simulations were seeded with a small quarter disk of solid at one corner of the lattice and a spatially uniform undercooling $u = -\Delta$. To reduce the computational time, simulations were performed only in the quadrant $x > 0$ and $y > 0$. Care has to be taken that the diffusion field along the direction of growth does not reach the end of the computational box. One way of accomplishing this is to choose a box size that can accommodate the final fully converged dendrite and its diffusion field. This would require large box sizes and hence long simulation times. Instead, we have chosen to periodically translate the phase and diffusion fields a certain distance in the direction opposite to the growth of the tip. This procedure allows us to compute the dendrite tip in a smaller box and leads to a significant speed up of the simulations. We have checked that the results we report here are independent of this translation.

The simulations reported here are for the fixed values $W_0 = 1$ and $\tau_0 = 1$. Note, however, that we can always rescale space and time such that the only independent parameters that appear in the phase-field equations are α and λ . We have kept W_0 and τ_0 in the equations to keep dimensions explicit for clarity of exposition.

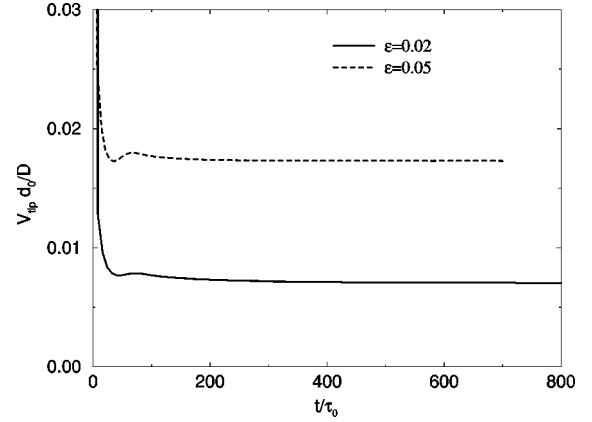


FIG. 4. Dimensionless tip velocity as a function of time for two choices of ϵ_4 and $\Delta = 0.55$ and $\Delta x/W_0 = 0.4$.

The interface is defined as the contour for which $\psi = 0$. The tip velocity V_{tip} was calculated from the position of the $\psi = 0$ point along the growth direction. It was allowed to reach a steady-state value after which the simulation was ended. Plots of the dimensionless tip velocity $\vec{V}_{\text{tip}} = V_{\text{tip}} d_0 / D$ vs time for two different values of ϵ_4 are shown in Fig. 4.

To select the grid spacing Δx for our simulations, we decreased $\Delta x/W_0$ in steps of 0.1 until V_{tip} did not change in value by more than 2%. In Fig. 5 we plot \vec{V}_{tip} vs $\Delta x/W_0$ for the two choices of $h(\psi)$ along with the value obtained from the Green function calculation. The two choices correspond to the IVF and the VF, respectively (i.e., $h_{\text{IVF}}(\psi) = \psi$ and $h_{\text{VF}}(\psi) = 15(\psi - 2\psi^3/3 + \psi^5/5)/8$ for which Eqs. (87) and (88) also reduce to the entropy formulation [5] used in the computations of Refs. [14,17]). Figure 5 shows clearly that the IVF converges more rapidly than the VF. Furthermore, although not shown here, we have found that for high V the VF can produce an unphysical spurious branch of steady-state growth solutions. For these reasons we have chosen to perform our computations with the IVF and $\Delta x/W_0 = 0.4$.

Let us now consider the convergence of our results as a function of the computational parameters. For this, we first note that, for $\beta = 0$, d_0 and D can be scaled out completely

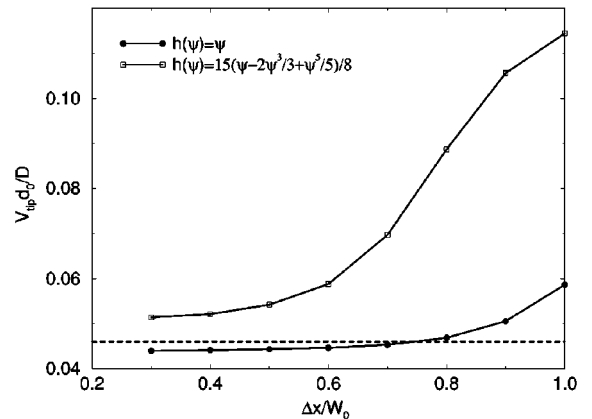


FIG. 5. Dimensionless tip velocity as a function of grid spacing for two choices of $h(\psi)$ for $\Delta = 0.65$, $\epsilon_4 = 0.05$, and $d_0/W_0 = 0.554$. The dashed line corresponds to the value obtained from the Green function calculation.

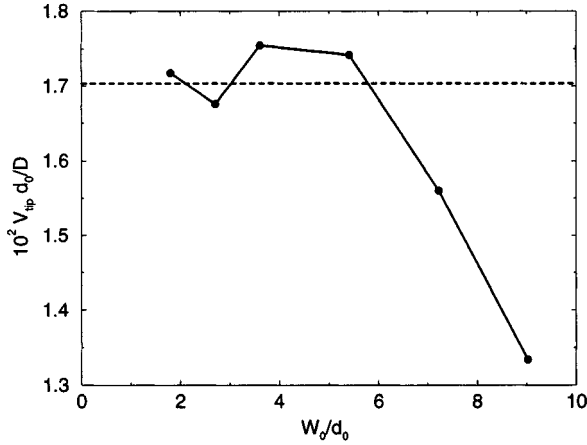


FIG. 6. Dimensionless tip velocity as a function of W_0/d_0 for $\Delta=0.55$ and $\epsilon_4=0.05$. As in Fig. 5 the dashed line corresponds to the value obtained from the Green function calculation.

from the free-boundary problem of dendritic growth by measuring length and time in units of d_0 and d_0^2/D , respectively. This implies that the dimensionless tip velocity and tip radius are functions of undercooling and anisotropy only and can be written as

$$\tilde{V}_{\text{tip}} = \frac{V_{\text{tip}} d_0}{D} = F_V(\Delta, \epsilon_4), \quad (92)$$

$$\tilde{\rho}_{\text{tip}} = \frac{\rho_{\text{tip}}}{d_0} = F_\rho(\Delta, \epsilon_4). \quad (93)$$

Next, recall that the derivation of the thin-interface limit is based on treating $p = W_0/\ell_c$ as small parameter. Therefore the convergence of our results can be established by decreasing the parameters $p_{\text{tip}} \equiv W_0 V_{\text{tip}}/D$ or $\kappa_{\text{tip}} \equiv W_0/\rho_{\text{tip}}$, and checking that \tilde{V}_{tip} and $\tilde{\rho}_{\text{tip}}$ converge to fixed values. Another way to check convergence is to compare the interface shape to the exact shape as we shall do below. In practice, convergence was achieved by decreasing D and concomitantly decreasing $\lambda^* \sim D$ via Eq. (91) to keep $\beta=0$. Since V_{tip} and ρ_{tip} are proportional to D/d_0 and d_0 , respectively, and since d_0 is proportional to W_0/λ^* , decreasing D is equivalent to decreasing simultaneously $p_{\text{tip}} = W_0 V_{\text{tip}}/D$ and $\kappa_{\text{tip}} = W_0/\rho_{\text{tip}}$. It is also equivalent to decreasing the ratio W_0/d_0 and showing that our results are independent of interface thickness. We took as a satisfactory measure of convergence that \tilde{V}_{tip} does not vary by more than a few percent upon decreasing W_0/d_0 . A typical convergence result is shown in Fig. 6. Finally, a typical sequence of dendritic patterns is shown in Fig. 7, where we plot the $\psi=0$ contour every 5000 iterations.

It is possible to benchmark the results of our phase-field code *quantitatively* since the theory of the operating state of the dendrite tip is well established in 2D. The steady-state growth problem can be solved numerically to any desired precision, giving predictions of the dendrite tip velocity and the steady-state interface shape. To obtain these steady states, Eqs. (3), (4), and (62) are first written in the moving frame (moving with a velocity V_{tip}) and then recast into a single integral equation by the standard Green function

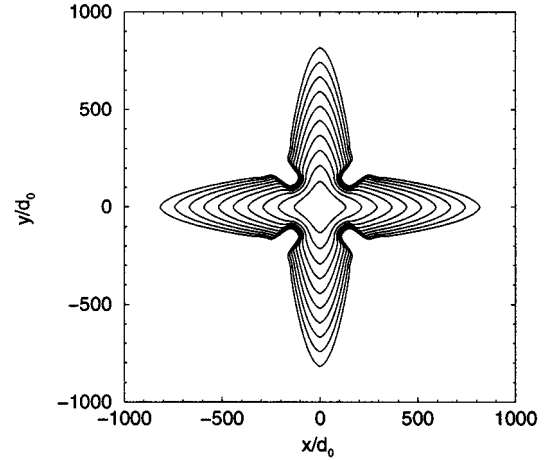


FIG. 7. Sequence of interface shapes shown every 5000 iterations for the parameter values $\Delta=0.65$, $\epsilon_4=0.05$, $d_0/W_0=0.554$, and $\Delta t/\tau_0=0.075$.

method. This equation was first written down by Nash and Glicksman [63] and takes the form

$$\Delta - d_0(\mathbf{n})\kappa - \beta(\mathbf{n})V_{\text{tip}}\cos\bar{\theta} = \int_{-\infty}^{+\infty} \frac{dx'}{2\pi l} \exp\left[\frac{y(x) - y(x')}{l}\right] K_0\left[\frac{|r - r'|}{l}\right], \quad (94)$$

where $l \equiv 2D/V_{\text{tip}}$ is the diffusion length. Several groups [37–39] have solved Eq. (94) and shown that it admits a discrete spectrum of solutions if a finite amount of anisotropy, in either the surface energy [37–39] or the interface kinetics [41], is present. Only the fastest growing solution in this discrete set is stable and corresponds to the dynamically selected operating state of the dendrite tip [44,46].

To benchmark our simulation results, we solved numerically the steady-state growth problem defined by Eq. (94). The input parameters of these calculations were chosen to correspond exactly to those of the phase-field computations; namely, $\beta(\mathbf{n})=0$, d_0 defined by Eq. (82), and $a_s(\mathbf{n})$ defined by Eq. (83). A comparison of the dimensionless steady-state tip velocities obtained by phase-field simulations and Green's function calculations is shown in Table II. A comparison of interface shapes for two different undercoolings is shown in Fig. 8.

It can be seen that the quantitative agreement is remarkably good over the whole range of d_0 , Δ , and ϵ_4 investigated here. Table II shows that accurate simulations are still possible at a very small d_0/W_0 ratio with an enormous gain in computational efficiency in agreement with the estimate of the computation time given by Eq. (9).

B. With kinetics

Above we have chosen the computational parameters such that the kinetic coefficient vanishes but we can also perform simulations with a nonzero kinetic coefficient. As an example we have simulated a kinetically controlled dendrite with an isotropic surface energy [i.e., $W(\mathbf{n})=W_0$] and a finite kinetic anisotropy. The kinetic anisotropy was introduced by choosing $\tau(\mathbf{n}) = \tau_0[1 + \tilde{\epsilon}_{\text{kin}}(n_x^4 + n_y^4)]$. If this form is substituted into Eq. (63), we obtain

TABLE II. Comparison of steady-state tip velocities calculated by phase-field simulations (\tilde{V}_{tip}) and calculated by the Green function method ($\tilde{V}_{\text{tip}}^{\text{GF}}$). T_{CPU} denotes the CPU time in hours for simulations on a DEC Alpha 3000-700 workstation. T_{CPU} on one processor of the Cray C90 is roughly five times smaller. The relevant computational and material parameters are $W_0=1$, $\tau_0=1$, $\Delta x/W_0=0.4$, $\Delta t/\tau_0=0.016$, and $h(\psi)=\psi$. λ is chosen equal to λ^* defined by Eq. (91) to simulate kinetic-free growth.

| Δ | ϵ_4 | D | d_0/W_0 | \tilde{V}_{tip} | $\tilde{V}_{\text{tip}}^{\text{GF}}$ | % error | N_x | N_y | T_{CPU} |
|----------|--------------|-----|-----------|--------------------------|--------------------------------------|---------|-------|-------|------------------|
| 0.65 | 0.05 | 1 | 0.554 | 0.0465 | 0.0469 | 1 | 600 | 300 | 2 |
| 0.55 | 0.05 | 2 | 0.277 | 0.0168 | 0.0170 | 1 | 800 | 200 | 4 |
| 0.55 | 0.05 | 3 | 0.185 | 0.0175 | 0.0170 | 3 | 600 | 200 | 1 |
| 0.55 | 0.05 | 4 | 0.139 | 0.0174 | 0.0170 | 2 | 400 | 150 | 0.2 |
| 0.50 | 0.05 | 3 | 0.185 | 0.01005 | 0.00985 | 2 | 1000 | 200 | 3 |
| 0.45 | 0.05 | 3 | 0.185 | 0.00557 | 0.00545 | 2 | 1000 | 300 | 14 |
| 0.45 | 0.05 | 4 | 0.139 | 0.00540 | 0.00545 | 1 | 800 | 250 | 5 |
| 0.30 | 0.05 | 10 | 0.055 | 0.00064 | 0.00068 | 6 | 1200 | 400 | 25 |
| 0.25 | 0.05 | 13 | 0.043 | 0.00027 | 0.00028 | 4 | 4000 | 1000 | 100 |
| 0.60 | 0.03 | 2 | 0.277 | 0.0183 | 0.0188 | 3 | 600 | 300 | 5 |
| 0.55 | 0.02 | 2 | 0.277 | 0.00735 | 0.00685 | 6 | 800 | 400 | 10 |

$$\beta(\mathbf{n}) = \bar{\beta}[1 + \epsilon_{\text{kin}}(n_x^4 + n_y^4)], \quad (95)$$

where $\bar{\beta}$ and ϵ_{kin} are functions of τ_0 , λ , and $\tilde{\epsilon}_{\text{kin}}$ which can be easily derived using Eq. (63). For our simulations, we have chosen these parameters such that $\bar{\beta}=0.6$ and $\epsilon_{\text{kin}}=0.05$. The results are presented in Table III. The quantitative agreement is again within a few percent as expected.

VI. THREE-DIMENSIONAL EQUATIONS AND LATTICE ANISOTROPY

A. Basic equations

The Gibbs-Thomson condition takes the form

$$u_i = -d_0 \sum_{i=1,2} [a_s(\mathbf{n}) + \partial_{\theta_i}^2 a_s(\mathbf{n})]/R_i - \beta(\mathbf{n})V, \quad (96)$$

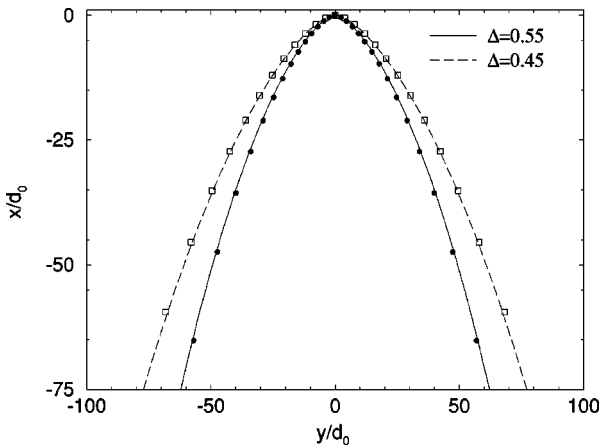


FIG. 8. Comparison of steady-state tip shapes calculated by phase-field simulations (lines) and the Green function method (symbols) for $\epsilon_4=0.05$. The two interfaces correspond to $\Delta=0.55$, $d_0/W_0=0.277$ (solid line and circles), and $\Delta=0.45$, $d_0/W_0=0.185$ (dashed line and squares). The time step in both simulations was $\Delta t/\tau_0=0.016$. For clarity, only one out of every four symbols along the interface is shown for the Green function results.

where the underlying cubic symmetry of the surface energy is expressed by $a_s(\mathbf{n})$,

$$\begin{aligned} a_s(\mathbf{n}) &= \bar{a}_s[1 + \epsilon'(n_x^4 + n_y^4 + n_z^4)] \\ &= \bar{a}_s[1 + \epsilon'(\cos^4 \bar{\theta} + \sin^4 \bar{\theta} \{1 - 2\sin^2 \bar{\phi} \cos^2 \bar{\phi}\})]. \end{aligned} \quad (97)$$

Here $\bar{\theta}$ and $\bar{\phi}$ are the standard spherical angles that the normal to the solid-liquid interface, and its projection in the x - y plane, make with respect to the z axis and the x axis, respectively. The constants \bar{a}_s and ϵ' can again be related to the usual measure of the anisotropy strength ϵ_4 using Eqs. (85) and (86).

The corresponding phase-field equations take the form

$$\partial_t u = D \nabla^2 u + \partial_t \psi / 2, \quad (98)$$

$$\begin{aligned} \tau(\mathbf{n}) \partial_t \psi &= [\psi - \lambda u(1 - \psi^2)](1 - \psi^2) + \vec{\nabla} \cdot [W(\mathbf{n})^2 \vec{\nabla} \psi] \\ &+ \partial_x \left(|\vec{\nabla} \psi|^2 W(\mathbf{n}) \frac{\partial W(\mathbf{n})}{\partial (\partial_x \psi)} \right) \\ &+ \partial_y \left(|\vec{\nabla} \psi|^2 W(\mathbf{n}) \frac{\partial W(\mathbf{n})}{\partial (\partial_y \psi)} \right) \\ &+ \partial_z \left(|\vec{\nabla} \psi|^2 W(\mathbf{n}) \frac{\partial W(\mathbf{n})}{\partial (\partial_z \psi)} \right), \end{aligned} \quad (99)$$

TABLE III. Comparison of steady-state tip velocities calculated by phase-field simulations (\tilde{V}_{tip}) and calculated by the Green function method ($\tilde{V}_{\text{tip}}^{\text{GF}}$) for the pure kinetic dendrite. The relevant computational and material parameters are $W_0=1$, $\lambda=4.42$, $D=1$, $\tau_0=5.77$, $\Delta x/W_0=0.4$, $\Delta t/\tau_0=0.0577$, $\epsilon_{\text{kin}}=0.05$.

| Δ | d_0/W_0 | \tilde{V}_{tip} | $\tilde{V}_{\text{tip}}^{\text{GF}}$ | % error |
|----------|-----------|--------------------------|--------------------------------------|---------|
| 0.85 | 0.20 | 0.0202 | 0.0206 | 2 |
| 0.80 | 0.20 | 0.0142 | 0.0136 | 4 |

where we have chosen $h(\psi) = \psi$ and

$$W(\mathbf{n}) = W_0(1 - 3\epsilon_4) \left[1 + \frac{4\epsilon_4}{1 - 3\epsilon_4} \frac{(\partial_x \psi)^4 + (\partial_y \psi)^4 + (\partial_z \psi)^4}{|\vec{\nabla} \psi|^4} \right] \quad (100)$$

corresponding to a cubic anisotropy as in Eq. (97). As in our 2D simulations, we will use $W_0 = 1$ in all our 3D simulations.

All spatial derivatives were discretized using Δx^2 accurate finite difference formulas. The Laplacians $\nabla^2 \psi$ and $\nabla^2 u$ were discretized using the six-point nearest-neighbor formula:

$$\Delta x^2 \nabla^2 \psi \approx \psi_{i+1jk} + \psi_{i-1jk} + \psi_{ij+1k} + \psi_{ij-1k} + \psi_{ijk+1} + \psi_{ijk-1} - 6\psi_{ijk}, \quad (101)$$

where the indices (i, j, k) measure position along the (x, y, z) axes, respectively. The cross partial derivatives were discretized using the four-point formula

$$(4\Delta x^2) \partial_{xy}^2 \psi \approx \psi_{i+1j+1k} - \psi_{i+1j-1k} - \psi_{i-1j+1k} + \psi_{i-1j-1k}, \quad (102)$$

with similar formulas for $\partial_{xz}^2 \psi$ and $\partial_{yz}^2 \psi$. Time stepping was done using a first-order Euler scheme. The simulations were performed on a cubic grid of size $N_x \times N_y \times N_z$ with a constant grid spacing Δx . Because of the cubic symmetry only an octant is sufficient to provide the full shape of the dendrite. Simulations were started with a small spherical seed in the corner of the octant and with a spatially uniform undercooling $u = -\Delta$.

B. Lattice anisotropy

In this section we describe a numerical procedure that incorporates corrections to the surface tension and kinetic anisotropy due to the discreteness of the lattice. This procedure makes it possible to choose Δx larger than needed to fully resolve the spatial derivatives in the interfacial region where ψ varies rapidly on the scale of W as well as to resolve smaller anisotropies. While anisotropies larger than a few percent are relatively easy to simulate, values smaller than 1% become difficult to resolve because of the contribution of the grid anisotropy. The fact that the lattice has the same cubic symmetry as the crystal can be exploited to define an effective anisotropy that includes the contribution of the underlying grid.

There is of course a limit to how large Δx can be chosen that is set by the onset of oscillations in the interface position on the scale of the lattice. These oscillations, which are due to the pinning effect of the lattice on the interface, have been analyzed in a pioneering paper by Cahn [64], and further studied numerically by Reynolds and co-workers [65]. In practice, we have found that accurate simulation results can be obtained by our procedure if Δx is chosen about twice larger than needed to resolve accurately the continuum limit of the phase-field equation. This is demonstrated explicitly for dendritic growth in 2D. For this value of Δx , the lattice oscillations appear to be sufficiently small not to produce spurious sidebranching. The increase in Δx by a factor of 2

reduces the simulation time by a factor of about 2^5 in 3D since $t_{\text{sim}} \sim (\Delta x/d_0)^{-(2+d)}$ in d dimensions and allows us to resolve an anisotropy of surface tension as small as 2/3 of a percent with about 10% accuracy.

1. Surface energy

To calculate the effective surface tension anisotropy, defined here as ϵ_e , we simulate the 3D equilibrium shape produced by the phase-field model with a given value of ϵ_4 input in the function $W(\mathbf{n})$ defined by Eq. (100). We then match this shape to the theoretical shape of an equilibrium crystal in the sharp-interface theory [60], which can be expressed in Cartesian coordinates as [66]

$$x = R_0 [f(\bar{\theta}, \bar{\phi}) \sin(\bar{\theta}) \cos(\bar{\phi}) + \partial_{\bar{\theta}} f(\bar{\theta}, \bar{\phi}) \cos(\bar{\theta}) \cos(\bar{\phi}) - \partial_{\bar{\phi}} f(\bar{\theta}, \bar{\phi}) \sin(\bar{\phi}) / \sin(\bar{\theta})], \quad (103)$$

$$y = R_0 [f(\bar{\theta}, \bar{\phi}) \sin(\bar{\theta}) \sin(\bar{\phi}) + \partial_{\bar{\theta}} f(\bar{\theta}, \bar{\phi}) \cos(\bar{\theta}) \sin(\bar{\phi}) + \partial_{\bar{\phi}} f(\bar{\theta}, \bar{\phi}) \cos(\bar{\phi}) / \sin(\bar{\theta})], \quad (104)$$

$$z = R_0 [f(\bar{\theta}, \bar{\phi}) \cos(\bar{\theta}) - \partial_{\bar{\theta}} f(\bar{\theta}, \bar{\phi}) \sin(\bar{\theta})], \quad (105)$$

where

$$f(\bar{\theta}, \bar{\phi}) = 1 + \frac{4\epsilon_e}{1 - 3\epsilon_e} [\cos^4 \bar{\theta} + \sin^4 \bar{\theta} (1 - 2\sin^2 \bar{\phi} \cos^2 \bar{\phi})] \quad (106)$$

and $(\bar{\theta}, \bar{\phi})$ are as before the spherical angles of the normal to the solid-liquid interface. To determine ϵ_e we then match the phase-field and theoretical shapes in the y - z plane. This is simply done by measuring on the cross section of the 3D phase-field shape in this plane the radial distances from the origin to the interface ($\psi = 0$) along the y axis, R_{10} , and along the $y = z$ line, R_{11} , and substituting these distances in the expression

$$\epsilon_e = \frac{R_{10}/R_{11} - 1}{R_{10}/R_{11} + 1}, \quad (107)$$

which is simple to work out. Note that this procedure only works well in practice because the underlying grid has the *same* cubic symmetry as the lattice. For this reason, the entire 3D phase-field shape can be accurately fitted by the equations above with a simple cubic anisotropy, as shown in Fig. 9.

One practical detail is worth mentioning. The phase-field equilibrium shape is simulated by only evolving ψ with a spherical solid inclusion of radius R_0 as initial condition. The temperature field is kept constant in space, and chosen initially equal to the critical undercooling for which this equilibrium shape would neither shrink nor grow if the surface energy were isotropic (i.e., $\Delta = d_0/R_0$). This undercooling is then slightly adjusted in time by a feedback mechanism that maintains the velocity of the interface, measured along some arbitrary axis, equal to zero (i.e., Δ is increased by some small amount if the crystal shrinks and decreased if it

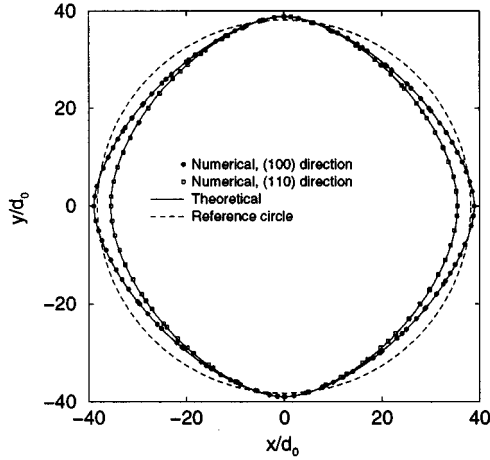


FIG. 9. Phase-field simulated equilibrium shapes in the (100) plane (solid circles) and the (110) plane (open squares) and the theoretical shapes for the corresponding ϵ_e (solid lines) for the grid spacing $\Delta x/W_0=0.8$. The anisotropy used as input into the phase-field equations is $\epsilon_4=0.05$ whereas the effective anisotropy obtained by fitting to the theoretical equilibrium shape is $\epsilon_e=0.047$. The dashed line shows a circle corresponding to an isotropic solid inclusion for reference.

grows). This procedure is dynamically stable and selects automatically the exact undercooling for which the crystal neither shrinks nor grows.

Results of our equilibrium shape phase-field simulations are illustrated in Fig. 9 where we show the numerically obtained shapes in the (100) plane (solid circles) and in the (110) plane (open squares) for the grid spacing $\Delta x/W_0=0.8$ used in our 3D computations of the next section. The theoretical equilibrium shapes calculated with ϵ_e in the (100) and (110) plane are drawn as solid lines and are seen to agree very well with the simulated shapes. We have also drawn for reference a dashed line that represents a circle corresponding to an isotropic solid inclusion.

In order to check whether the effective anisotropy depends on the size of the seed crystal, the procedure to calculate ϵ_e was repeated for different R_0 . As can be seen in Fig. 10, the effective anisotropy depends weakly on R_0 . For all

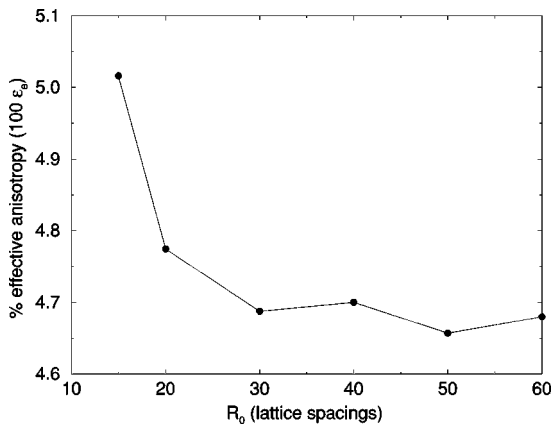


FIG. 10. The effective anisotropy ϵ_e that includes the small correction of the lattice anisotropy as a function of the radius R_0 of the equilibrium shape for $\epsilon_4=0.05$ and for the grid spacing $\Delta x/W_0=0.8$.

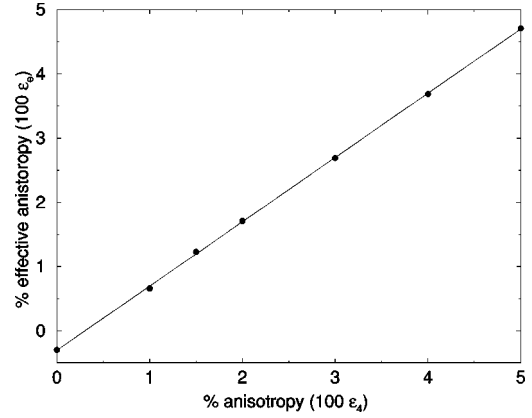


FIG. 11. The effective anisotropy ϵ_e that includes the small correction of the lattice anisotropy as a function of the anisotropy parameter ϵ_4 that is used as input into the phase-field equations for the grid spacing $\Delta x/W_0=0.8$. The solid line is a linear fit through the data points.

values of ϵ_4 investigated here, we have taken the value ϵ_e corresponding to $R_0=40$ lattice units. This value was motivated by the averaged observed tip radius in our simulations. Note though that, in the entire range $R_0=15-60$, ϵ_e does not vary by more than about 6% of its mean value. This represents the accuracy to which we can determine the effective anisotropy. Values of ϵ_e for various ϵ_4 can be found in Table V. Finally, in Fig. 11 we plot ϵ_e as a function of ϵ_4 for the range of anisotropies we have used in this paper. The data are well fitted with a linear fit indicating that the grid anisotropy is constant and independent of the input anisotropy.

As will be shown elsewhere [67], it turns out that one can also analytically derive a relation between ϵ_e and ϵ_4 of the form

$$\epsilon_e = \epsilon_4 - a\Delta x^2 + O(\epsilon_4\Delta x^2) + O(\Delta x^4), \quad (108)$$

where a is a numerical constant that depends on the choice of the function $f(\psi)$. This result is obtained by writing the discretized Laplacian as the sum of $\nabla^2\psi$, which is rotationally invariant, and the higher-order term proportional to $\Delta x^2(\partial_x^4 + \partial_y^4 + \partial_z^4)\psi$, which has a cubic symmetry and modifies the surface tension anisotropy. For $f(\psi)$ defined by Eq. (17), $a=1/240$, such that Eq. (108) gives an excellent agreement with the values of ϵ_e obtained by fitting the equilibrium shapes.

2. Interface kinetics

In Sec. III we derived an analytical expression for the anisotropic kinetic coefficient $\beta(\mathbf{n})$ in the thin-interface limit [Eq. (63)]. For the value $\Delta x/W_0=0.8$ used in our 3D computations, there are lattice corrections to the kinetic coefficient, and thus to the function $\tau^*(\mathbf{n})$ and the parameter λ^* that make $\beta(\mathbf{n})$ vanish. It is possible to incorporate quantitatively these corrections as long as Δx is within a certain range where time-periodic oscillations of the interface velocity on the scale of the lattice spacing remain of sufficiently small amplitude. The basic strategy consists of developing a method to calculate the planar interface velocity on a discrete lattice in a range of Δx where these oscillations are negligibly small. This procedure can then be readily extended to

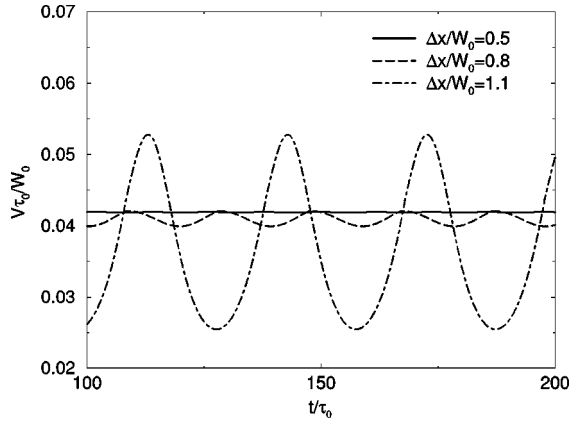


FIG. 12. Interface velocity as a function of time for the front solution of Eq. (110) for different values of $\Delta x/W_0$ and $\Delta=0.02$.

calculate an effective kinetic coefficient, $\beta_e(\mathbf{n})$, and therefore an effective function, $\tau_e^*(\mathbf{n})$, and constant λ_e^* , which make $\beta_e(\mathbf{n})$ vanish.

To illustrate the nature of these velocity oscillations it is useful to first consider the simple front problem defined by

$$\tau_0 \partial_t \psi = W_0^2 \partial_x^2 \psi + \psi - \psi^3 - u. \quad (109)$$

This problem corresponds to the purely kinetic controlled motion of a planar interface, without diffusion, where the dimensionless interfacial undercooling u is constant and set to $u = -\Delta$. In the continuum limit, this equation has a constant velocity traveling wave solution $\psi(x, t) = \psi(x - Vt)$ moving in the $+x$ direction for $u < 0$, where $V \sim -u$ for small $|u|$. On a discrete lattice, with a centered finite difference representation of the spatial derivative, Eq. (109) becomes

$$\partial_t \psi_i = \frac{1}{\Delta x^2} (\psi_{i+1} + \psi_{i-1} - 2\psi_i) + \psi_i - \psi_i^3 - u, \quad (110)$$

where $\psi_i(t)$ denotes the value of $\psi(x, t)$ at $x = i\Delta x$, and we have set $W_0 = \tau_0 = 1$ for simplicity. This equation is discrete in space and continuous in time. Treating time as a continuous variable is justified because the interface velocity is small $V \ll 1$ (i.e., $V = \alpha p$ in units where $\tau_0 = W_0 = 1$). Consequently, the error made in calculating $\partial_t \psi$ with an Euler scheme scales as $\partial_t^2 \psi \Delta t$, or $V^2 \partial_x^2 \psi \Delta t$. Furthermore, since the stability of the scheme requires one to choose $\Delta t \sim \Delta x^2/2d$ in d dimension, this error scales as $V^2 \partial_x^2 \psi \Delta x^2/2d$. It is therefore smaller by a factor of $V^2/2d$ than the error made in the spatial discretization, which scales as $\partial_x^2 \psi \Delta x^2$. Therefore, for all practical purposes, t can be treated as a continuous variable as long as V is small.

Equation (110) also has a moving front solution, but with an interface velocity which oscillates in time for large Δx because the lattice acts as an effective periodic potential in which the interface is riding. Furthermore, this periodic potential tends to pin the interface. Consequently, for a given undercooling, there exists a critical value of the lattice spacing, Δx_c , at which the interface becomes completely pinned and stalls [64,65]. This pinning is illustrated here in Figs. 12, 13(a), and 13(b). These results were obtained by integrating

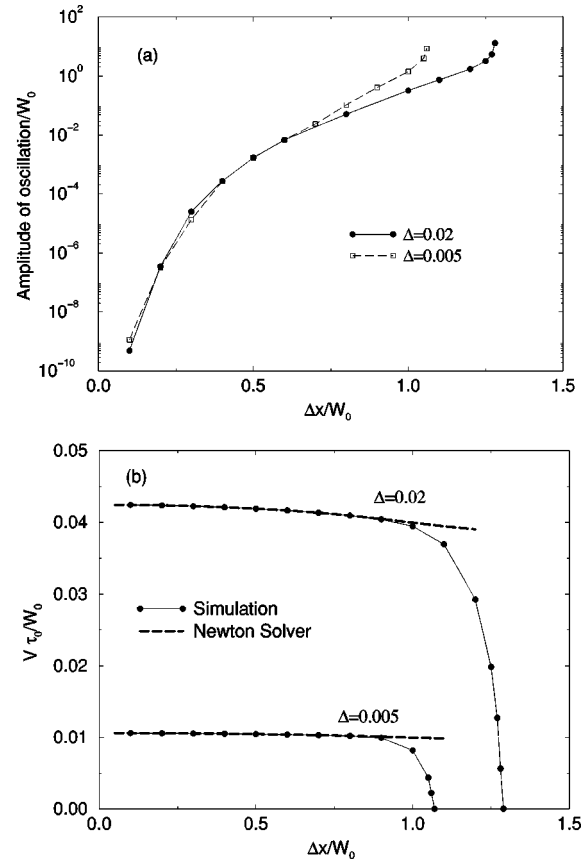


FIG. 13. Plots as a function of $\Delta x/W_0$ of (a) the relative amplitude of oscillation, defined as the ratio of the difference between the maximum and minimum interface velocity during one period of oscillation and the average velocity, and (b) the average interface velocity calculated by the direct numerical integration of Eq. (110) (solid line and filled circles) and by the approximate theory (Newton solver) that neglects the effect of velocity oscillations.

Eq. (110) with an explicit Euler scheme and a time step $\Delta t/\tau_0 = 0.005$. The interface position $X(t)$ was calculated by using a fourth-order accurate interpolation formula to interpolate where $\psi = 0$. The instantaneous interface velocity $V \equiv dX(t)/dt$ was approximated by the formula $[X(t + \Delta t) - X(t - \Delta t)]/(2\Delta t)$. The average interface velocity V_{av} was defined as the time-averaged velocity, or equivalently as the total distance traveled by the interface during one oscillation period, ΔX , divided by the period of the oscillation T : $V_{av} \equiv \Delta X/T$. Finally, the relative oscillation amplitude is defined as $A = (V_{max} - V_{min})/V_{av}$, where V_{max} and V_{min} are, respectively, the maximum and minimum interface velocity during one period.

The results of Fig. 13 show that there are two contributions of the lattice, which dominate in different ranges of Δx . The first, which is dominant over a range of Δx smaller than Δx_c [corresponding to where the solid and dashed lines overlap in Fig. 13(a) and the solid line has a slope equal to 2 in Fig. 14] is a slow decrease of V_{av} due to the correction of $O(\Delta x^2)$ made in approximating $\partial_x^2 \psi$ by a finite difference formula. This quadratic dependence on Δx is shown in Fig. 14 where we show a log-log plot of $V_{av}(\Delta x/W_0 = 0) - V_{av}(\Delta x/W_0)$ vs $\Delta x/W_0$. This behavior is unrelated to the pinning effect of the lattice and is already present in a range

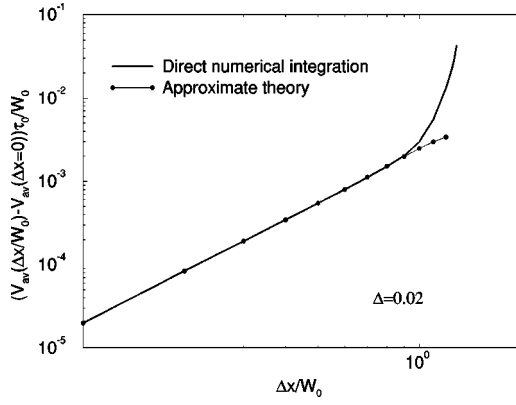


FIG. 14. Plot of $V_{\text{av}}(\Delta x/W_0=0) - V_{\text{av}}(\Delta x/W_0)$ vs $\Delta x/W_0$ for $V_{\text{av}}(\Delta x/W_0)$ obtained by direct numerical integration of Eq. (110) and by the approximate theory (Newton solver) that neglects the effect of velocity oscillations (solid line and filled circles).

of Δx where the oscillation amplitude is negligibly small. The second effect of the lattice is the pinning that becomes dominant as Δx approaches Δx_c . The latter is associated with a relatively abrupt vanishing of the interface velocity and occurs in a range of Δx where the oscillation amplitude A becomes of order unity.

The key point here is that it is possible to choose Δx relatively large and still have a negligibly small oscillation amplitude, in which case V is essentially independent of time and equal to V_{av} . Thus it is possible to perform more efficient computations with a larger Δx while still having an interface that behaves dynamically as if space was continuous. This, however, requires one to know how to calculate V_{av} in order to make contact with the thin-interface limit. One way to compute V_{av} is to simulate Eq. (110) directly, which becomes somewhat cumbersome when u is allowed to diffuse, which is the case we need to consider to calculate $\beta_e(\mathbf{n})$ as described below. Another way, which explicitly excludes the contribution of the lattice oscillations, is to reduce Eq. (110) to a time-independent problem by exploiting the discrete translation symmetry of the moving front solution of Eq. (110):

$$\psi_i(t+jT) = \psi_{i-j}(t), \quad (111)$$

where as before $T = \Delta x/V_{\text{av}}$ is the oscillation period. This problem can then be solved as in Sec. III by using a Newton solver for the unknown ψ and V_{av} . This is the equivalent to making a transformation to a moving frame as in the continuum case, albeit for a case where ψ is only known at a discrete set of points. The simplest possible approximation of $\partial_t \psi_i$ that only involves the nearest neighbors is $\partial_t \psi_i \approx V_{\text{av}}(\psi_{i-1} - \psi_{i+1})/(2\Delta x)$. This approximation, however, is not useful here because it is itself only accurate to $O(\Delta x^2)$. Using it would defeat the purpose of the present procedure which is to calculate the $O(\Delta x^2)$ corrections to V_{av} induced by the spatial discretization. Therefore we calculate $\partial_t \psi_i$ by using the expression

$$\partial_t \psi_i = V_{\text{av}} \partial_x \psi|_{x=i\Delta x},$$

which is exact if we neglect the oscillations, and evaluate $\partial_x \psi$ to spectral accuracy. Since the interface is not periodic,

i.e., ψ varies between $+1$ and -1 over the interval $x \in [-d, d]$, we construct a new interface over the interval $x \in [-d, 3d]$ that consists of the original interface plus its mirror image about the point $x=d$. This new interface is then periodic and can be Fourier transformed to calculate $\partial_x \psi$ in Fourier space using the relation $(\partial_x \psi)_k = ik\psi_k$. The inverse Fourier transform of $(\partial_x \psi)_k$ is then evaluated to obtain $\partial_x \psi|_{x=i\Delta x}$ to spectral accuracy. The results are of course independent of d for $d/W \ll 1$. As shown in Figs. 13 and 14, this procedure gives extremely accurate values of V_{av} as a function of Δx and only breaks down when the oscillation amplitude becomes non-negligible.

The extension of the above procedure to calculate the effective kinetic coefficient $\beta_e(\mathbf{n})$, as well as λ_e^* and $\tau_e^*(\mathbf{n})$ is straightforward. This kinetic coefficient can be conveniently defined as the limit

$$\beta_e(\mathbf{n}) = \lim_{\Delta \rightarrow 1} \frac{\Delta - 1}{V_{\text{av}}(\mathbf{n})} \quad (112)$$

of the discrete-space analog of the 1D planar front problem studied in Sec. IV. In this definition $V_{\text{av}}(\mathbf{n})$ denotes the average velocity of the interface for growth along a direction parallel to \mathbf{n} that is calculated as outlined above by neglecting the effect of the lattice oscillations and therefore the pinning to the lattice. [Note that the limit in Eq. (112) is not defined if the pinning effect of the lattice is included since the interface will always get pinned in the $[100]$ direction at some small enough $\Delta - 1$ for any finite Δx . This is of course not a limitation since we are only interested in calculating $\beta_e(\mathbf{n})$ in a regime where Δx is such that these oscillations are small.]

Because of the cubic symmetry, it is sufficient to calculate $\beta_e(\mathbf{n})$ along two principal crystallographic directions (e.g., $[100]$ and $[110]$) to determine λ_e^* and $\tau_e^*(\mathbf{n})$ and the value of $\beta_e(\mathbf{n})$ along an independent direction (e.g., $[111]$) can then be used as a self-consistency check that λ_e^* and $\tau_e^*(\mathbf{n})$ make $\beta_e(\mathbf{n})$ vanish in all growth directions.

The discrete-space equations of motion of the planar interface along the $[100]$, $[110]$, and $[111]$ directions can be readily obtained from the discretized version of the 3D phase-field equations [Eqs. (98) and (99)] by assuming that ψ has the same value at *all* the lattice points contained within the corresponding (100), (110), and (111) plane, respectively, that are perpendicular to these growth directions. This is exact if we neglect the effect of the lattice oscillations in which case the planar interface translates uniformly along these directions. The corresponding 1D equations are defined by

$$\partial_t u = \frac{D}{h^2} (u_{i+1} + u_{i-1} - 2u_i) + \partial_t \psi / 2, \quad (113)$$

$$\begin{aligned} \tau \partial_t \psi = & [\psi - \lambda u (1 - \psi^2)] (1 - \psi^2) + \left(\frac{KW_0}{h} \right)^2 \\ & \times (\psi_{i+1} + \psi_{i-1} - 2\psi_i), \end{aligned} \quad (114)$$

TABLE IV. Parameters τ , K , and h , entering in Eqs. (113) and (114) for different growth directions.

| \mathbf{n} | τ | K | h |
|--------------|-------------------------|---------------------|---------------------|
| [100] | $\tau_0(1 + \delta)$ | $1 + \epsilon_4$ | Δx |
| [110] | $\tau_0(1 - \delta)$ | $1 - \epsilon_4$ | $\Delta x/\sqrt{2}$ |
| [111] | $\tau_0(1 - 5\delta/3)$ | $1 - 5\epsilon_4/3$ | $\Delta x/\sqrt{3}$ |

with the far-field boundary condition $u \rightarrow -\Delta$ far from the interface, where τ , h , and K depend on the growth direction and are listed in Table IV.

The effective kinetic function that makes $\beta_e(\mathbf{n})$ vanish is then defined as

$$\tau_e^*(\mathbf{n}) = \tau_0(1 - 3\delta) \left[1 + \frac{4\delta}{1 - 3\delta} (n_x^4 + n_y^4 + n_z^4) \right], \quad (115)$$

where the time constant τ_0 and the anisotropy parameter δ need to be determined together with λ_e^* . We determined these constants by requiring that $\tau_e(\mathbf{n})$ is equal to unity along the [100] direction, which yields the relation $\tau_0(1 + \delta) = 1$ between two of the three constants, and by further requiring that $\beta_e(\mathbf{n})$ vanishes along the [100] and [110] directions, which provides two additional independent constraints. A self-consistency check was performed by calculating the magnitude of $\beta_e(\mathbf{n})$ along the [111] direction, with these same values of τ_0 , δ , and λ_e^* . This check yielded a value of $\beta_{[111]} \sim 10^{-4}$ which is negligibly small. The results of our calculations are presented in Table V.

One last point should be emphasized. The procedure developed here works as long as the pinning effect of the lattice is negligible and the lattice oscillations remain small. For the value $\Delta x/W_0 = 0.8$ used in our 3D computations the relative oscillation amplitude measured at the dendrite tip is $A \sim 10^{-2}$ for the undercooling $\Delta = 0.45$, which is sufficiently small.

3. Numerical tests

To test the lattice effects induced by the large grid sizes and to verify our results obtained in Secs. VI A and VI B, we have performed 2D simulations for the grid spacings employed in our 3D work. The effective anisotropy in 2D is identical to the one in 3D since the equilibrium shape in the symmetry planes (e.g., the x - y plane) reduces to the equilibrium shape in 2D. The results of our 2D simulations are presented in Table VI. We also show in the table the tip velocity calculated by the solvability theory. The agreement is very satisfying and demonstrates that it is possible to ob-

TABLE V. A summary of the effective parameters for $D = 1$.

| $\Delta x/W_0$ | ϵ_4 | ϵ_e | λ_e^* | τ_0 | δ |
|----------------|--------------|--------------|---------------|----------|----------|
| 0.6 | 0.0081 | 0.0066 | 1.651 | 0.996 | 0.0038 |
| 0.8 | 0.015 | 0.0123 | 1.697 | 0.996 | 0.0038 |
| 0.8 | 0.020 | 0.0171 | 1.679 | 0.982 | 0.0183 |
| 0.8 | 0.030 | 0.0265 | 1.643 | 0.962 | 0.0400 |
| 0.8 | 0.040 | 0.0369 | 1.608 | 0.942 | 0.0615 |
| 0.8 | 0.050 | 0.0470 | 1.575 | 0.924 | 0.0828 |

TABLE VI. Comparison of steady-state tip velocities calculated by 2D phase-field simulations for $\Delta = 0.55$ (\bar{V}_{tip}) and calculated by the Green function method ($\bar{V}_{\text{tip}}^{\text{GF}}$) for the same Δ . The phase-field simulations were performed using ϵ_4 , $\tau_e(\mathbf{n})$, and λ_e^* as input. The Green function calculation was performed using the grid corrected anisotropy ϵ_e that corresponds to the ϵ_4 value used in the phase-field simulation.

| ϵ_e | $\Delta x/W_0$ | D | d_0/W_0 | \bar{V}_{tip} | $\bar{V}_{\text{tip}}^{\text{GF}}$ | % error |
|--------------|----------------|-----|-----------|------------------------|------------------------------------|---------|
| 0.0066 | 0.6 | 3 | 0.179 | 0.00221 | 0.00211 | 5 |
| 0.0171 | 0.8 | 3 | 0.176 | 0.00638 | 0.00627 | 2 |
| 0.0265 | 0.8 | 2 | 0.269 | 0.00968 | 0.00996 | 3 |
| 0.0369 | 0.8 | 1 | 0.550 | 0.01309 | 0.01340 | 2 |
| 0.0470 | 0.8 | 2 | 0.281 | 0.01728 | 0.01767 | 2 |

tain quantitative results with a larger grid spacing than needed to fully resolve the continuum limit using the procedure developed in this section.

VII. THREE-DIMENSIONAL SIMULATIONS

We have performed simulations for an undercooling $\Delta = 0.45$ and for an anisotropy ranging from $\epsilon_e = 0.0066$ to $\epsilon_e = 0.047$. Most of our 3D simulations were performed for $\Delta x/W_0 = 0.8$ with $\tau(\mathbf{n}) = \tau_e(\mathbf{n})$ given by Eq. (115) and the values of τ_0 , δ , and $\lambda = \lambda_e^*$ listed in Table V. For the lowest anisotropy, we have also carried out simulations with $\Delta x/W_0 = 0.6$. A smaller Δx was necessary in this case to resolve the anisotropy more accurately. The velocity of the tip was measured along the z axis and the simulation was stopped after this velocity reached a steady state. As in the 2D simulations, we periodically translated the computational box a certain distance behind the tip. The convergence of our numerical results with respect to the computational parameters was checked following the same procedure as in 2D. That is, for each value of the anisotropy we decreased D , and hence p_{tip} and κ_{tip} , until the dimensionless tip velocity did not change by more than a few percent. A typical convergence study is shown in Figs. 15(a) and 15(b) where we show, respectively, the dimensionless tip velocity and the dimensionless tip radius as a function of W_0/d_0 .

A. Tip selection

The operating state of the dendrite can be characterized by

$$\sigma^* = \frac{2Dd_0}{\rho_{\text{tip}}^2 V_{\text{tip}}}, \quad (116)$$

$$P = \frac{\rho_{\text{tip}} V_{\text{tip}}}{2D}, \quad (117)$$

where σ^* is the classic stability parameter that first appeared within the context of marginal stability theory, and P is the dendrite tip Péclet number. For $d_0 = 0$, P is given exactly by the Ivantsov relation for a paraboloid of revolution [68]

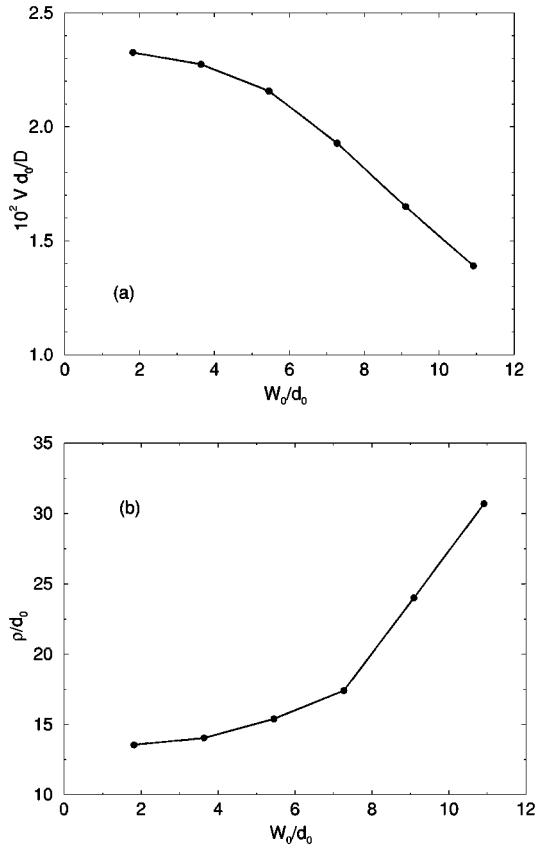


FIG. 15. Plots of the dimensionless interface velocity (a) and the dimensionless tip radius (b) as a function of W_0/d_0 for $\epsilon_e = 0.0369$ and $\Delta = 0.45$. The time step ranges from $\Delta t/\tau_0 = 0.07$ for the smallest value of W_0/d_0 to $\Delta t/\tau_0 = 0.01$ for the largest value of W_0/d_0 .

$$\Delta = P_{IV} \exp(P_{IV}) \int_{P_{IV}}^{\infty} dz \frac{\exp(-z)}{z}. \quad (118)$$

In the phase-field simulations, however, ρ_{tip} and V_{tip} are calculated independently to determine P and σ^* . The velocity was calculated, as in 2D (see Sec. V), from the position of the $\psi=0$ point along the growth direction. The details of the calculation of the curvature are described in Appendix B.

A simulated 3D morphology for a high anisotropy ($\epsilon_e = 0.047$) is shown in Fig. 16. There are six dendrite tips growing along the six $[100]$ directions. Furthermore, each dendrite has four “fins” that reflect the underlying cubic anisotropy. This picture should be contrasted with Fig. 17 which shows the result of a simulation with $\epsilon_e = 0$. Without anisotropy the interface undergoes a series of tip-splitting instabilities and no dendrites are formed. These simulation results confirm the essential role of anisotropy in dendritic growth. It is worth noting that it has recently been shown by phase-field simulation that there exist steady-state growth solutions in 3D for zero anisotropy in the form of triplons [23]. These solutions are directly analogous to doublons [27,69] in 2D and may therefore exist for arbitrarily small Δ , although this has not yet been demonstrated analytically as in 2D [69]. From this standpoint, one would be tempted to interpret the simulation of Fig. 17 as showing the early stage of formation of triplons, although a longer run would be necessary to con-

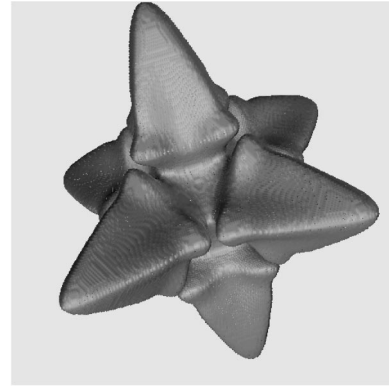


FIG. 16. Results of a typical 3D phase-field simulation on a $300 \times 300 \times 300$ cubic lattice for $\epsilon_e = 0.047$ which shows dendrite tips growing along the principal $\langle 100 \rangle$ directions. The solid-liquid boundary shown here corresponds to the $\psi=0$ surface reconstructed by reflection about the $x=y=z=0$ planes. The structure is seen from an angle where all six $\langle 100 \rangle$ directions are visible.

firm this supposition. We have not investigated this aspect further here and Figs. 16 and 17 are only intended to show that growth morphologies with and without anisotropy are qualitatively different.

Unlike in 2D, the steady-state growth equations of dendritic growth in 3D are too difficult to solve numerically by the boundary integral method for an arbitrary nonaxisymmetric shape. These equations, however, can be solved using the so-called axisymmetric approximation [49,50]. This approximation assumes that the anisotropy and the interface shape $z(r, \bar{\theta})$ are independent of the polar angle $\bar{\theta}$ in the x - y plane perpendicular to the growth axis. Averaging over this angle yields an effective anisotropy function of the form

$$a_s(\mathbf{n}) = \bar{a}_s (1 + \epsilon' [\cos^4 \bar{\theta} + \frac{3}{4} \sin^4 \bar{\theta}]), \quad (119)$$

where $\bar{\theta}$ is again the angle between the normal direction to the solid-liquid interface and the $[100]$ direction (growth axis). This axisymmetric approximation reduces the 3D steady-state growth problem to a tractable problem that is two dimensional. The equations can once again be transformed into a single integro-differential equation in which the interface shape $z(r)$ appears as an unknown and approaches the Ivantsov paraboloid of revolution far from the tip region [49,70]. This equation is defined by

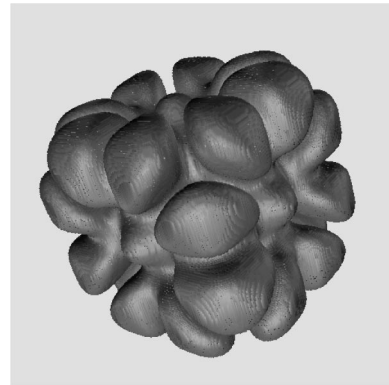


FIG. 17. Same as Fig. 9 but with $\epsilon_e = 0.0$.

TABLE VII. Dimensionless steady-state tip velocity and tip radius ($\tilde{\rho}_{\text{tip}} = \rho_{\text{tip}}/d_0$) calculated by 3D phase-field simulations. The relevant computational and material parameters are $W_0 = 1$, $h(\psi) = \psi$, and $\Delta = 0.45$. The time step varied from $\Delta t/\tau_0 = 0.018$ for the lowest anisotropy value to $\Delta t/\tau_0 = 0.076$ for the highest anisotropy value.

| ϵ_e | $\Delta x/W_0$ | D | d_0/W_0 | \tilde{V}_{tip} | $\tilde{\rho}_{\text{tip}}$ |
|--------------|----------------|-----|-----------|--------------------------|-----------------------------|
| 0.0066 | 0.6 | 3 | 0.179 | 0.00549 | 155.3 |
| 0.0123 | 0.8 | 2 | 0.261 | 0.00925 | 77.93 |
| 0.0171 | 0.8 | 2 | 0.264 | 0.0121 | 51.23 |
| 0.0265 | 0.8 | 1.5 | 0.359 | 0.0181 | 26.09 |
| 0.0369 | 0.8 | 1 | 0.550 | 0.0231 | 13.56 |
| 0.0470 | 0.8 | 0.5 | 1.124 | 0.0297 | 6.25 |

$$\Delta - \Delta_\mu = \int_0^{2\pi} \frac{d\phi'}{2\pi} \int_0^{+\infty} \frac{r' dr'}{l} \frac{\exp[(z(r') - z(r) - d)/l]}{d}, \quad (120)$$

where $l = 2D/V$ is the diffusion length,

$$d \equiv \{r^2 + r'^2 - 2rr' \cos(\phi - \phi') + [z(r') - z(r)]^2\}^{1/2},$$

and

$$\Delta_\mu = -d_0[a_s(\mathbf{n}) + \partial_{\bar{\theta}}^2 a_s(\mathbf{n})] \frac{z_{rr}}{(1+z_r^2)^{3/2}} - d_0[a_s(\mathbf{n}) + \cot \bar{\theta} \partial_{\bar{\theta}} a_s(\mathbf{n})] \frac{z_r}{(1+z_r^2)^{1/2}}$$

represents the axisymmetric Gibbs-Thomson shift. The tip radius and velocity, obtained by solving Eq. (120), were used to calculate σ^* and P . It is worth stressing that we calculate σ^* here using the tip radius. To our knowledge all previous studies have reported values of σ^* that are calculated with the Ivantsov tip radius. We will see below that the numerically obtained Péclet number P and the Ivantsov Péclet number P_{IV} defined by Eq. (118) differ significantly, even for relatively small anisotropies. Hence, for a meaningful comparison with experiment, care must be taken in defining σ^* with the actual tip radius. For completeness, we have also computed σ^* using the linear axisymmetric solvability theory of Barbieri and Langer [50] that is based on a linearization around the Ivantsov paraboloid of revolution. In this theory, $P = P_{\text{IV}}$, independent of the value of anisotropy.

The results of 3D computations are summarized in Tables VII and VIII and in Figs. 18 and 19. We also show for comparison the results of the numerical solvability theory [i.e., the numerical solution of Eq. (120)], and the linear solvability of Barbieri and Langer [i.e., the analytic solution of Eq. (120) with a shape linearized around the Ivantsov needle crystal]. We first note that the values of σ^* produced by our simulations are systematically higher than the values from the numerical solvability theory. For small anisotropy these values are still reasonably close but for anisotropies greater than about 3% the deviation between the phase-field results and the numerical solvability results become significant. Most likely, this does not indicate a breakdown of solv-

TABLE VIII. Result of phase-field simulations on a $200 \times 200 \times 400$ cubic lattice compared to the results of the numerical and linear solvability theories for $\Delta = 0.45$. A and η characterize the amplitude of the fourfold symmetry component of the tip morphology in simulations. Typical runs took 60–140 CPU hours on a DEC-ALPHA 3000-700 workstation and shorter times on a Cray-YMP and a Cray-T3D.

| ϵ_e | Phase-field simulations | | | | Solvability theory | | | |
|--------------|-------------------------|------------|--------|----------|--------------------|------------|-----------------|------------|
| | P | σ^* | η | A^{-1} | P | σ^* | P_{IV} | σ^* |
| 0.0066 | 0.426 | 0.015 | 1.78 | 13.0 | 0.418 | 0.0128 | 0.471 | 0.0116 |
| 0.0123 | 0.360 | 0.036 | 1.73 | 11.3 | 0.367 | 0.0329 | 0.471 | 0.0250 |
| 0.0171 | 0.312 | 0.063 | 1.68 | 10.1 | 0.324 | 0.0578 | 0.471 | 0.0367 |
| 0.0265 | 0.236 | 0.16 | 1.62 | 7.8 | 0.247 | 0.142 | 0.471 | 0.0602 |
| 0.0369 | 0.159 | 0.47 | 1.57 | 5.7 | 0.172 | 0.365 | 0.471 | 0.0890 |
| 0.0470 | 0.093 | 1.72 | 1.54 | 4.0 | 0.109 | 1.037 | 0.471 | 0.1240 |

ability theory, but of the axisymmetric approximation. This conclusion is supported by the fact that the fourfold deviation from a shape of revolution increases in magnitude with anisotropy (as described below). This $\cos 4\phi$ mode was previously found to affect very little the value of σ^* computed with a linearized shape for small ϵ_4 [49]. In contrast, our results indicate that for a surface tension anisotropy larger than about 3% the amplitude of this mode becomes sufficient to produce a large percental change in σ^* . We also do not observe any sidebranching [44,53,57,71] without adding noise to the phase-field equations. Hence our simulations rule out the possibility of a dynamical attractor other than a steady-state needle crystal.

The linear axisymmetric theory is seen to break down at much smaller anisotropy. This is because it assumes that the steady-state shape remains close to the Ivantsov paraboloid of revolution. Figure 19 shows that the actual Péclet number

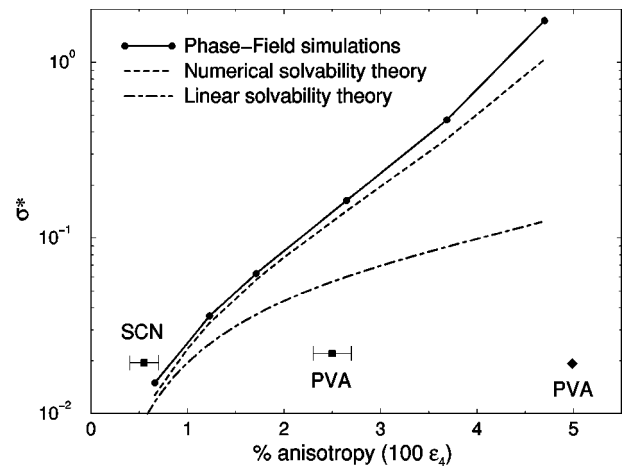


FIG. 18. Plot of σ^* vs ϵ_e for $\Delta = 0.45$ showing the results of phase-field simulations compared to the approximate predictions of the numerical and linear solvability theories. Also plotted are the small Δ experimental values of σ^* for SCN [57] and PVA [54] using the anisotropy measurements of Ref. [54] for PVA (filled diamond) and of Ref. [56] for SCN and PVA (filled squares and error bars).

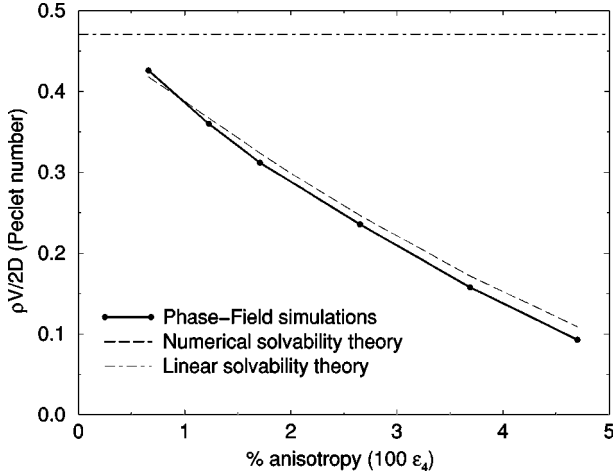


FIG. 19. Plot of P vs ϵ_e for $\Delta=0.45$ showing the results of phase-field simulations compared to the approximate predictions of the numerical and linear solvability theories.

already starts deviating significantly from its Ivantsov value P_{IV} at small anisotropy. The predictions of the Péclet number from the numerical solvability theory on the other hand remain relatively accurate over the entire range of anisotropy.

Figure 18 also shows a comparison between the numerical results and experimental data points for two materials. The comparison with experiments is limited to pivalic acid and succinonitrile that are the only pure materials with an underlying cubic symmetry for which detailed measurements of both anisotropy [53,54,56] and σ^* [53–55,57] are available. For a summary of experimental results on other materials and alloys we refer to Ref. [56].

There are two anisotropy measurements reported for PVA in the literature. However, if we use either the value measured by Muschol *et al.* [56], or the value measured by Huang and Glicksman [53], the measured value of σ^* [54,55] is still much smaller than both the phase-field and the numerical solvability values. A possible explanation for this discrepancy could be that interface kinetics is playing an essential role in the solidification of PVA. This is supported by the fact that σ^* was found to depend on the undercooling in both the experiments [55] and in the phase-field simulations for large undercooling [17]. The observed dependence [55], however, does not seem to be sufficient to explain the present discrepancy. A closer examination of kinetic effects for this material seems warranted.

We can also compare our phase-field results with measurements in succinonitrile. Glicksman and co-workers measured σ^* both in ground based experiments [53] and under microgravity conditions [57], where convection effects are minimized. Interestingly, both the ground based and the microgravity experiments give essentially the same value of σ^* : $\sigma^*=0.0192$ for terrestrial experiments and $\sigma^*=0.0196$ for microgravity experiments. It should be noted that although σ^* is nearly identical in both experiments, the velocities and tip radii differ significantly and it is only the dimensionless combination σ^* that is identical. The experimental value for σ^* is approximately 20% larger than the phase-field value $\sigma^*\approx 0.015$ but most of this discrepancy can be accounted for by the finite Péclet number correction. To evaluate this correction, we first note that, in the absence

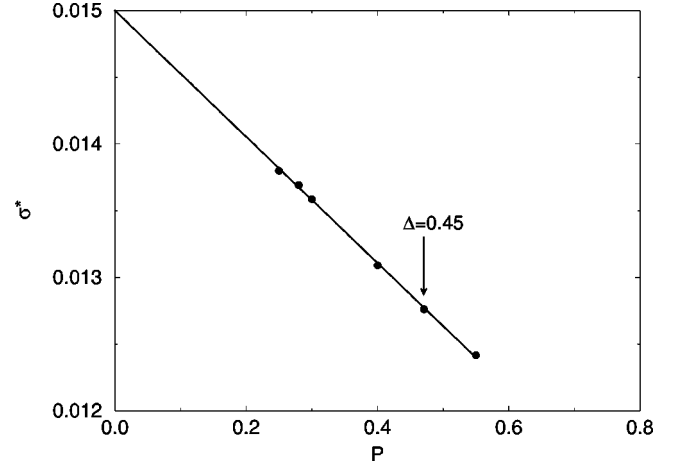


FIG. 20. Plot of σ^* vs P for the numerical axisymmetric solvability theory for $\epsilon_4=0.0066$. The solid line is a guide to the eye and demonstrates that the dependence on P of σ^* is linear. The data point with the arrow corresponds to the undercooling $\Delta=0.45$ at which the phase-field simulations are performed and shows that this value is approximately 15% smaller than the value for small undercoolings.

of kinetics, σ^* depends only on ϵ_4 and P , and can therefore be expanded for small P as

$$\sigma^*(P, \epsilon_4) = \sigma^*(0, \epsilon_4) + \frac{\partial \sigma^*}{\partial P}(0, \epsilon_4)P + \dots \quad (121)$$

This equation can then be used to extract the small Δ experimental limit of σ^* as long as we know both $\partial \sigma^*/\partial P$ and σ^* at some finite Δ . To make use of it, we have calculated this slope by calculating σ^* vs P using the numerical axisymmetric solvability code. The results are shown in Fig. 20. They indicate that the finite Péclet correction at $\Delta=0.45$ decreases σ^* by about 15% from its small Δ limiting value. Consequently, the value of σ^* obtained in our simulations should be increased by 15% to compare it with experiment, which yields a small Δ estimate of $\sigma^*\approx 0.017$. Furthermore, the effective anisotropy $\epsilon_e=0.0066$ lies inside the range of uncertainty of the measured value $\epsilon_4=0.0055\pm 0.0015$ for SCN [56]. Therefore we obtain a reasonably good agreement with experiment for SCN within the existing uncertainty in the measured value of anisotropy.

B. Tip morphology

Figures 21(b) and 21(d) show $\psi=0$ contours in the (100) planes that are equally spaced in the z direction by one tip radius. Close to the tip the shapes are nearly circular but further behind the tip the contours are clearly noncircular and the deviation from an axisymmetric shape becomes larger. Comparing Figs. 21(b) and 21(d) also reveals that the non-axisymmetric component of the tip morphology becomes larger for higher anisotropy. To analyze the steady-state morphology of the dendrite tip we used the Fourier decomposition

$$r^2(\phi, z) = \sum_n A_n(z) \cos 4n\phi, \quad (122)$$

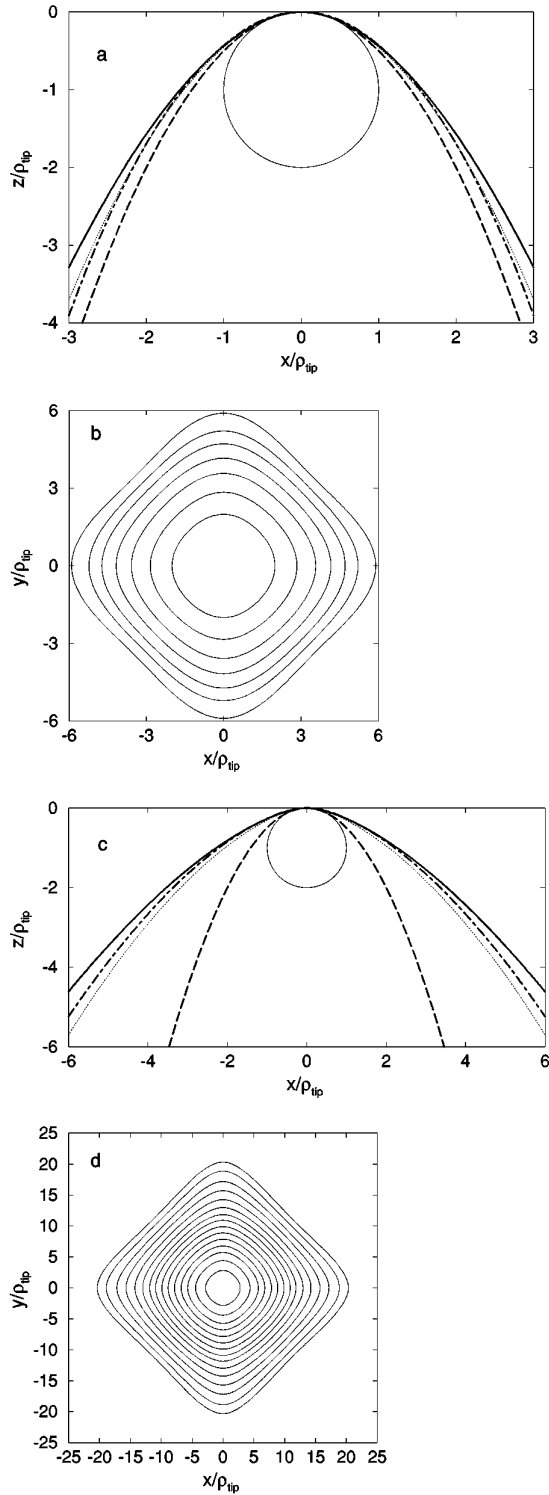


FIG. 21. Steady-state tip morphology for $\epsilon_e=0.0123$ (a) and (b) and for $\epsilon_e=0.0470$ (c) and (d). (a) and (c) show the interfaces in the $\phi=0^\circ$ (solid line) and $\phi=45^\circ$ (dash-dotted line) planes, and (b) and (d) show interfaces in the (100) planes equally spaced along z by one tip radius, with the first plane two tip radii from the tip. The Ivantsov parabola $z=-r^2/2$ (dashed line), the solution from the axisymmetric calculation (dotted line), and a circle of unit radius are superimposed in (a) and (c). The Fourier amplitudes at two tip radii behind the tip are in (b) $A_1(-2)=0.29$, $A_2(-2)=0.020$, and $A_3(-2)=0.0022$, and in (d) $A_1(-2)=0.73$, $A_2(-2)=0.077$, and $A_3(-2)=0.0095$, illustrating that the tip morphology is dominated by the fourfold symmetry mode.

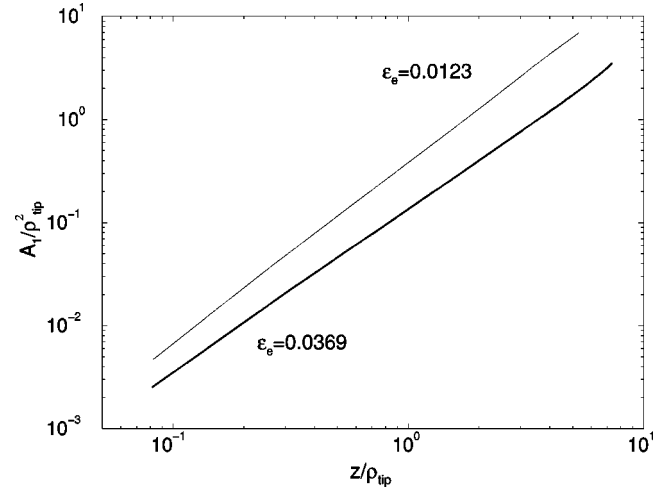


FIG. 22. Plot of the coefficients in the Fourier expansion coefficient A_1 vs the distance behind the tip z for two different anisotropies and for $\Delta=0.45$.

where r is the radial distance from the z axis. Both r and z are measured in units of ρ_{tip} with the tip at $z=0$. This decomposition has the advantage that it is general and does not presuppose a particular analytical form to fit the tip shape. The first term in the Fourier decomposition, $A_0(z)$, represents the axisymmetric contribution to the shape. It approaches a paraboloid of revolution, $A_0(z)=-2z$, for small $|z|$ and departs from this shape with increasing $|z|$. This can be seen in Figs. 21(a) and 21(c) where we have plotted as a dashed line the Ivantsov paraboloid [$r^2(z)=-2z$], together with the tip morphologies in the planes $\phi=0$ (solid line) and $\phi=45^\circ$ (dash-dotted line). These figures also show that this departure is more pronounced at larger anisotropy as one would expect.

The modes $A_n(z)$ for $n \geq 1$ are responsible for the non-axisymmetric departure from a shape of revolution. The first nonaxisymmetric mode $A_1(z)$ was found to be much larger than all the other modes indicating that the shape is dominated by the $\cos(4\phi)$ term. Furthermore, this mode can be described for all anisotropies by the power law $A_1(z)=A|z|^\eta$. This can be seen in Fig. 22 where we have plotted on a log-log scale $A_1(z)$ vs $|z|$ with $|z|$ ranging from $|z| \sim 0.1\rho_{\text{tip}}$ to $z \sim 5\rho_{\text{tip}}$ for two different anisotropies. For smaller z , our numerical interpolation is not sufficient to resolve accurately these amplitudes because the radius of the cross-sectional shape becomes only a few times, or comparable to, the lattice spacing. However, the analyticity of the 3D tip shape imposes that $\eta \rightarrow 2$ in the limit of $|z| \rightarrow 0$, such that the behavior $A_1(z)=A|z|^\eta$ cannot strictly extend all the way to $z=0$. So we expect that there should be, for $A_1(z)$, a crossover from a behavior in $|z|^\eta$, with $\eta \neq 2$, to $|z|^2$ very near the tip. The values of A and η in Table VIII clearly show that the amplitude of the fourfold symmetry mode is sensitively dependent on anisotropy, which is, as far as we know, a qualitatively novel aspect of our results. The linear solvability calculation of Ben Amar and Brener [51] and subsequent refinement by Brener and Melnikov [72] predicts that for small ϵ_4 the tip morphology should be independent of anisotropy, with $A^{-1}=12$ and $\eta=2$ for small $|z|$. The values of A and η listed in Table VIII indicate that this

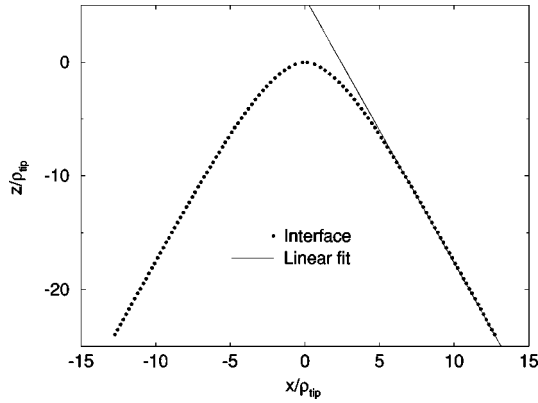


FIG. 23. Longitudinal cross section of phase-field simulated interface in the $\phi=0^\circ$ plane (solid circles) and a linear fit of the tail shape far behind the tip (solid line) for $\Delta=0.7$ and $\epsilon_e=0.0269$. For clarity only one out of six symbols is plotted.

prediction is most likely only valid for values of ϵ_4 which lie outside the range of experimental interest. This is also consistent with the fact that their calculation is only valid in the limit where $\sigma^* \sim \epsilon_4^{7/4}$, and that this 7/4 power law scaling is not yet attained at our smallest computed anisotropy.

In Figs. 21(a) and 21(c) we have also plotted as dotted lines the dendrite shape calculated by the numerical axisymmetric approach. As expected this axisymmetric approximation yields a solution that lies in between the shapes in the $\phi=0$ and $\phi=45^\circ$ planes and that deviates more strongly from the full numerical simulation for higher anisotropies.

Experimental data on the tip morphology are limited to NH_4Br [73] and SCN [74]. For NH_4Br dendrites it was found that the tip morphology is indeed well described by a single $\cos 4\phi$ mode. For SCN on the other hand, more modes seem to be necessary to fit the tip morphology which makes a direct comparison with the numerical values of η and A impossible. The origin of this difference, which is potentially due to noise amplification, remains to be understood.

C. Tail morphology

In a recent paper, Brener has derived a theory of the tail shape of 3D needle crystals [52]. His theory is based on the assumption that the cross sections of 3D steady-state needle crystals should grow as time-dependent 2D growth shapes away from the tip. With length measured in units of ρ_{tip} , his theory predicts that $|z| \sim r^{5/3}$ in an intermediate region where $1 \ll |z| \ll 1/P$, the exponent 5/3 having been derived by Almgren *et al.* for 2D Laplacian growth [75], and $|z| \sim r$, in the far tail region where $|z| \gg 1/P$. In this last region, the 2D time-dependent interface grows with a constant steady-state growth velocity that we shall denote here by V_{2D} in order to distinguish it from the steady-state growth velocity of the 3D needle crystal that we denote by V_{3D} . With these definitions, Brener's theory predicts that the tail region is described by the simple relation

$$r = B|z|, \quad (123)$$

with $B = V_{2D}/V_{3D}$, this relation being strictly valid for $B \ll 1$. In our 3D phase-field computations, Δ , and thus P are not quite small enough to distinguish the intermediate region

TABLE IX. Results of steady-state growth velocities obtained by 2D (V_{2D}) and 3D (V_{3D}) phase-field simulations as well as the measured slope obtained by fitting a straight line through the longitudinal cross section of the 3D needle crystal in the tail region (Fig. 23). Note the excellent agreement between the predicted slope V_{2D}/V_{3D} and the measured slope.

| Δ | ϵ_e | V_{2D} | V_{3D} | V_{2D}/V_{3D} | Slope |
|----------|--------------|----------|----------|-----------------|-------|
| 0.7 | 0.0269 | 0.0450 | 0.103 | 0.44 | 0.43 |
| 0.65 | 0.0269 | 0.0416 | 0.105 | 0.39 | 0.40 |

where $|z| \sim r^{5/3}$. It is, however, possible to distinguish the far tail region described by Eq. (123).

Figure 23 shows an interface in the $\phi=0^\circ$ plane for $\Delta=0.7$ as solid circles. Far away from the tip it can be seen that the interface approaches a straight line. A linear fit to this tail, shown as a solid line, was found to have a slope of ~ 0.43 . To test Eq. (123) we have calculated the velocity of the 3D dendrite as well as the velocity of the 2D dendrite. The values for the dimensionless velocities obtained from 2D and 3D simulations are given in Table IX. We see that the ratio of the 2D and 3D velocities is very close to the slope of the linear fit. In Table IX we also give the results of a simulation for $\Delta=0.65$. Again, the ratio and the slope are nearly identical, demonstrating that, far behind the tip, the growth in the cross section perpendicular to the growth direction is effectively 2D.

To illustrate more clearly that the fins in the (100) planes grow as 2D dendrites, we show in Fig. 24 as solid circles cuts in the (100) plane of our 3D simulations. The cuts are, as in Figs. 21(b) and 21(d), equally spaced along the growth direction by one tip radius. If the tail shape can be described by Eq. (123) then 3D cuts spaced by one tip radius are equivalent to 2D interfaces spaced *in time* by ρ_{tip}/v_{2D} . Figure 24 shows that the interface shapes for a 2D simulation

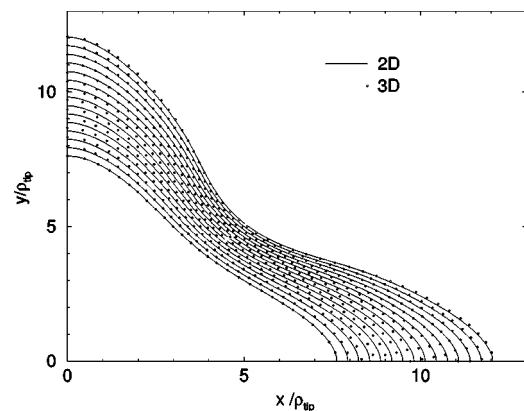


FIG. 24. Transverse cross sections of 3D phase-field simulated needle crystal in the (100) plane equally spaced along the z axis (solid circles) by one 3D tip radius ρ_{tip} . Superimposed for comparison are 2D interfaces (solid lines) obtained by 2D phase-field simulations equally spaced in time by ρ_{tip}/V_{2D} . The 2D time-dependent simulation uses as input the interface profile and the temperature field of the 3D cross section closest to the tip in the present figure. Both 3D and 2D simulations are for the same parameters as in Figs. 21(b) and 21(d). The first interface plotted is $\sim 15\rho_{\text{tip}}$ away from the tip. For clarity, only one quadrant of the cross section is shown.

for the same computational parameters spaced as described above are nearly identical to the 3D cuts. The slight deviation of the shapes is due to the fact that the slope is not quite constant yet.

We close this section with a few observations. First, it is somewhat surprising that we observe a linear tail shape with a slope predicted by Eq. (123), and obtain such a good match between 3D cross sections and 2D time-dependent growth shapes in Fig. 24. This is because Brener's analogy is strictly only valid if $V_{2D}/V_{3D} \ll 1$, in which case the flux of temperature along the interface becomes negligible. In our simulations, this ratio is about 0.4. Apparently, this value is already small enough to suppress any 3D effects for the growth of the fins that already behave as 2D growth shapes. Second, it is unlikely that the linear tail shape will be observed experimentally. Most likely, the amplification of thermal noise will induce sidebranching before the linear regime can be reached. The generation of sidebranches is currently under investigation by phase-field simulation.

VIII. DISCUSSION

In this paper we have given a detailed exposition of a thin-interface limit of the phase-field equations describing the crystallization of a pure melt where the interface thickness is assumed to be small compared to the mesoscale of the solidification pattern, but non-vanishing. We have presented simulation results in 1D, 2D, and 3D, that demonstrate how this limit can be implemented to obtain accurate quantitative solutions of the time-dependent free-boundary problem. Computations in 1D and 2D have mainly been used to benchmark our method against exact predictions of the classical sharp-interface theory, whereas 3D simulations were performed to test the validity of solvability theory and gain new insights into the factors that determine the shape and operating state of actual dendrites observed in experiment.

Two aspects of the asymptotics are worth emphasizing.

(i) By a suitable choice of computational parameters we can simulate the solidification of a pure melt in the absence of kinetics. This, in turn, makes it possible to simulate the important limit where kinetic effects at the interface are negligible.

(ii) We can perform simulations for a larger interface thickness to capillary length ratio W/d_0 than was possible before. Since the computational time in d dimensions can be shown to scale as $\sim (W/d_0)^{-(d+2)}$, an increase in W/d_0 leads to an enormous gain in computational efficiency.

As a first test case, we used the method to model the growth of a planar front for undercoolings $\Delta > 1$. The solution of this problem is well known analytically and the velocity is only a function of Δ and the kinetic parameter β . Phase-field simulations that exploit the thin-interface limit were found to converge well to the results of the classical sharp-interface theory, and more efficiently than with the standard asymptotics of the phase-field model. As a second, and less trivial test case, we showed that the phase-field method can yield accurate predictions of the operating state of the 2D dendrite tip. For undercoolings as low as $\Delta = 0.25$ we were able to perform simulations with zero kinetics that were converged in numerical parameters. This convergence was achieved by decreasing W/d_0 until the dimen-

sionless velocity did not change by more than a few percent. These simulations provided us with both the velocity and the radius of the dendrite tip. It should be emphasized that, in contrast to previous phase-field studies, our results were compared directly to exact benchmarks of solvability theory obtained independently by Green's function method both with and without interface kinetics. The comparisons showed that the phase-field method was able to produce the correct velocities and tip radii with a relative error $< 5\%$. In addition, we found that the computation time decreased dramatically as the ratio W/d_0 was increased.

Our simulations were performed without employing more involved numerical techniques such as adaptive grids. Of course, the implementation of such techniques will speed up our calculations even further. This is especially the case for low undercoolings where the diffusion length becomes extremely large and the calculation of the diffusion field becomes very costly.

Our asymptotics have enabled us to perform quantitative simulations in 3D. To reduce the computation time even further than permitted by these asymptotics, we have used a somewhat larger grid spacing Δx than needed to fully resolve the continuum limit of the phase-field equations. The small surface tension grid anisotropy introduced by using a larger spacing (about 0.3% for $\Delta x/W_0 = 0.8$) was calculated by comparing the equilibrium 3D crystal shape produced by the phase-field model with the known analytic expression for a sharp interface. A methodology was also developed to calculate the grid-induced kinetic anisotropy and determine model parameters for which the kinetic coefficient vanish. These two steps allowed us to perform simulations of dendritic growth that are converged in computational parameters. This convergence was achieved as in 2D by decreasing W/d_0 until σ^* did not change by more than 10%.

We used our simulations to critically test microscopic solvability theory. We first compared our results to the linear axisymmetric solvability theory of Barbieri and Langer [50] which assumes that the underlying shape of the dendrite is the Ivantsov paraboloid and linearizes around that shape. We showed that this theory breaks down at large anisotropies and is presumably accurate for very small anisotropies only. Next, we compared our results to the nonlinear axisymmetric solvability theory which assumes that the dendrite is axisymmetric. This assumption leads to an effectively two-dimensional problem that can be solved numerically. Our simulations showed that this numerical solvability theory breaks down for much larger values of anisotropies. For values smaller than 3% the discrepancy between the simulations and the numerical solvability theory is approximately 30%.

In addition to the velocity and the tip radius of the 3D dendrite, we have also calculated the tip morphology. We found that for all values of anisotropy studied here the morphology is dominated by the fourfold mode and that the interface shape can be adequately represented by

$$r^2(\phi, z) = A_0(z) + A|z|^\eta \cos(4\phi) + \dots \quad (124)$$

The values of A and η on the other hand are strongly dependent on the anisotropy. A recent analytical linear solvability calculation by Ben Amar and Brener [51] predicts that both A and η should be independent of anisotropy in the limit of

small ϵ_4 . Our results suggest that the range of validity of their approximate theory lies outside the range of values of ϵ_4 that we simulated here, and at the margin of what is experimentally measurable.

We compared our simulations with values for σ^* reported in the experimental literature. For PVA the agreement between theory and experiment remains very poor [54,55]. There is a large discrepancy between the experimental values of PVA and the ones obtained from our phase-field simulations as well as the numerical solvability theory. The most likely explanation for this discrepancy is the dominant role of interface kinetics in this material that remains to be modeled quantitatively in 3D.

The comparison between our results and SCN is much more favorable. The smallest anisotropy value used in our study lies within the range of uncertainty of the experimental value for ϵ_4 . Our numerical value of σ^* is approximately 20% lower than the experimental value. To be able to perform our simulations the undercooling was chosen significantly higher than in experiments. This difference in undercooling between the simulation and the experiment accounts for most of the discrepancy in the value of σ^* . Therefore it is fair to argue that agreement between the experimental value for SCN and the numerical value is good.

Finally, we analyzed the shape of the dendrite tail far behind the tip. We find that the tail, at distances larger than the diffusion length, is well described by the linear relationship

$$r = \frac{V_{2D}}{V_{3D}} |z|, \quad (125)$$

where V_{2D} , V_{3D} are, respectively, the 2D and 3D steady-state dendrite tip velocities at the same undercooling. This means that the evolution in space of transverse cross sections of 3D steady-state needle crystals, with increasing distance behind the tip, is described by the evolution in time of a 2D growth shape. This result is in good agreement with the recent analytical theory of Brener [52].

Our results in 3D leave little doubt about the validity of microscopic solvability theory in describing needle crystals computed with a phase-field model and yield a relatively good quantitative agreement with experiment for SCN. Caution, however, is still needed in applying this theory to experiments until a proper explanation of the disagreement between theory and experiment, most likely due to kinetic effects, is obtained for PVA. Our simulations demonstrate the critical role of anisotropy in the selection of the operating state of the dendrite tip. The values of σ^* are reasonably close to the axisymmetric solvability theory, at least for small anisotropy. For higher anisotropy ($\epsilon_4 > 3\%$), the discrepancy between our simulations and the axisymmetric theory increases. However, this is not due to a failure of microscopic theory but due to the axisymmetric approximation.

The asymptotics we have presented in this paper can be applied to a variety of problems. We are currently including thermal fluctuations quantitatively in the phase-field model to investigate noise-induced sidebranching. We have also extended the present asymptotics to the directional solidifica-

tion of a dilute binary alloy. This makes it possible to investigate a number of interesting microstructural pattern formation issues.

ACKNOWLEDGMENTS

This research was supported by DOE Grant No. FG02-92ER45471 and we benefited from supercomputer time allocation at NERSC. We wish to thank Rob Almgren for valuable discussions about mathematical aspects of the present asymptotics, Herbert Levine for providing us with the 2D solvability code, Martine Ben Amar for performing cross checks of our 3D solvability calculations, Efim Brener and Heiner Müller-Krumbhaar for useful remarks, and Stuart Levy of the Geometry Center at the University of Minnesota for his gracious help in visualizing our results.

APPENDIX A: ASYMPTOTICS OF THE THIN-INTERFACE LIMIT

In this appendix, we show how the Gibbs-Thomson condition obtained in Sec. III can be rederived from a matched asymptotic expansion that treats λ as a small parameter. We start by rewriting the phase-field equations by making the dependence on λ explicit, i.e., by substituting $W = \lambda d_0/a_1$ and $\tau = \lambda^2 \beta_0 d_0/a_1^2$, which yields

$$\lambda^2 \frac{\beta_0 d_0}{a_1^2} \partial_t \psi = \lambda^2 \frac{d_0^2}{a_1^2} \nabla^2 \psi - f_\psi - \lambda g_\psi u, \quad (A1)$$

$$\partial_t u = D \nabla^2 u + \partial_t h/2. \quad (A2)$$

We then look for solutions of the form

$$u = u_0 + \lambda u_1 + \lambda^2 u_2 + \dots, \quad (A3)$$

$$\tilde{u} = \tilde{u}_0 + \lambda \tilde{u}_1 + \lambda^2 \tilde{u}_2 + \dots \quad (A4)$$

in the inner and outer regions, respectively, with a similar expansion for ψ in both regions. In the outer region, all the \tilde{u}_j ($j=0,1,2,\dots$) simply obey the diffusion equation $\partial_t \tilde{u}_j = D \nabla^2 \tilde{u}_j$ since the phase-field ψ is constant. In the inner region, the analog of Eqs. (31) and (32), rewritten in terms of the inner variable $\eta \equiv (\xi_3/\lambda)(a_1/d_0)$, become

$$\lambda \left[\frac{\beta_0}{a_1} V + \frac{d_0}{a_1} \left(\frac{1}{R_1} + \frac{1}{R_2} \right) \right] \partial_\eta \psi + \partial_\eta^2 \psi - f_\psi - \lambda g_\psi u = 0, \quad (A5)$$

$$\frac{\lambda d_0}{a_1} \left[V + D \left(\frac{1}{R_1} + \frac{1}{R_2} \right) \right] \partial_\eta u + D \partial_\eta^2 u - \frac{\lambda d_0}{a_1} V \partial_\eta h/2 = 0, \quad (A6)$$

where we have neglected the contributions of the partial derivatives $\partial_t \psi$ and $\partial_t u$ evaluated at fixed η that turn out to be unimportant at the end of the calculation. Substituting Eqs. (A3) and (A4) into Eqs. (A5) and (A6), we recover at zeroth order the stationary interface profile $\psi_0(\eta)$, defined by Eq. (35), and $u_0 = \text{const}$. For all higher orders in λ , Eq. (A6) yields a linear equation $\mathcal{L} \psi_j = F_j$ where \mathcal{L} is the linear operator defined by Eq. (38). Since \mathcal{L} is self-adjoint and satis-

fies $\mathcal{L}\partial_\eta\psi_0=0$, there is at each order in λ a solvability condition for the existence of a nontrivial solution ψ_j , given by

$$\int_{-\infty}^{+\infty} d\eta F_j \partial_\eta \psi_0 = 0. \quad (\text{A7})$$

The rest of the calculation is straightforward. At first order ($j=1$) Eq. (A7) yields

$$u_0 = -d_0 \left(\frac{1}{R_1} + \frac{1}{R_2} \right) - \beta_0 V, \quad (\text{A8})$$

which is the condition obtained previously by Caginalp [32]. At second order ($j=2$), we obtain

$$F_2 = - \left[\frac{\beta_0}{a_1} V + \frac{d_0}{a_1} \left(\frac{1}{R_1} + \frac{1}{R_2} \right) \right] \partial_\eta \psi_1 + \frac{f_{\psi\psi}^0}{2} \psi_1^2 + g_{\psi\psi}^0 \psi_1 u_0 + g_{\psi}^0 u_1, \quad (\text{A9})$$

where

$$u_1 = \bar{u}_1 + A \eta + \frac{d_0 V}{2Da_1} \int_0^\eta d\eta' h^0 \quad (\text{A10})$$

is obtained by solving Eq. (A6) at first order in λ and the constant \bar{u}_1 is determined by Eq. (A7). As before, if f and g are even and odd functions of ψ , respectively, \bar{u}_1 does not depend on A . In addition, it is easy to verify that all the terms on the right-hand side of Eq. (A9), except the last one, are proportional to odd functions of η since $\psi_1(\eta)$ is an even function of η . Therefore they give vanishing contributions to the solvability condition of Eq. (A6) at second order in λ . Finally, matching inner and outer solutions up to first order in λ we obtain the standard heat conservation condition, together with the interface condition

$$u_i \equiv \lim_{\xi_3 \rightarrow 0^\pm} [\bar{u}_0(\xi_3) + \lambda \bar{u}_1(\xi_3)] = -d_0 \left(\frac{1}{R_1} + \frac{1}{R_2} \right) - \beta_0 \left[1 - \lambda \frac{a_2 d_0}{D\beta_0} \right] V, \quad (\text{A11})$$

which is easily seen to be identical to Eq. (57) derived in Sec. III A in an asymptotic expansion that treats p as a small parameter. Note that, although the results are the same, the solvability conditions that yield the correction to the kinetic coefficient do not have identical forms because they appear at different orders in the two asymptotic expansions [i.e., Eq. (41) in Sec. III A and Eq. (A7) for $j=2$ here].

APPENDIX B: CALCULATION OF THE TIP RADIUS

The tip radius of the dendrite growing along the z axis was calculated in the y - z ($\phi=0^\circ$) plane. The expression for the curvature of the interface defined by $\psi=0$ is given at the tip by

$$\kappa_{\text{tip}} = \frac{1}{\rho_{\text{tip}}} = \frac{\partial_y^2 \psi(0,0,z_{\text{tip}})}{\partial_z \psi(0,0,z_{\text{tip}})}. \quad (\text{B1})$$

For the typical grid spacing $\Delta x/W_0=0.8$ used in our 3D computations, evaluating the derivatives in the expression above directly with the values of ψ on the lattice points would introduce a large error in κ_{tip} , especially since the tip does not usually coincide with a lattice point. For this reason we calculated these derivatives by interpolation.

We first fitted the function $\psi(0,0,z)$ in the neighborhood of the tip using a fourth-order polynomial $\tilde{\psi}(z)$. We used the five vertical lattice points closest to the tip along the z axis at $x=y=0$. This allowed us to calculate the tip position defined by $\tilde{\psi}(z_{\text{tip}})=0$, and then $\partial_z \psi(0,0,z_{\text{tip}}) = d\tilde{\psi}(z)/dz|_{z=z_{\text{tip}}}$.

Let us denote the z coordinates of the five points used to fit $\tilde{\psi}(z)$ by z_n for $n \in [1,5]$. We then fitted the functions $\psi(0,y,z_n)$ using fourth-order polynomials $\tilde{\psi}_n(y)$ for $n \in [1,5]$. For each n , we performed this fit using the five horizontal lattice points defined by $\psi(0,\pm m\Delta x,z_n)$ for $m \in [0,2]$ [where $\psi(0,m\Delta x,z_n) = \psi(0,-m\Delta x,z_n)$ by symmetry]. We then calculated $\partial_y^2 \psi(0,0,z_n) = d^2 \tilde{\psi}_n(y)/dy^2|_{y=0}$. Finally, we fitted the function $\partial_y^2 \psi(0,0,z)$ using a fourth-order polynomial through these five points and used this polynomial to calculate $\partial_y^2 \psi(0,0,z_{\text{tip}})$.

-
- [1] J. S. Langer, in *Directions in Condensed Matter* (World Scientific, Singapore, 1986), p. 164.
 - [2] G. J. Fix, in *Free Boundary Problems: Theory and Applications*, edited by A. Fasano and M. Primicerio (Piman, Boston, 1983), Vol. II, p. 580.
 - [3] J. B. Collins and H. Levine, *Phys. Rev. B* **31**, 6119 (1985).
 - [4] O. Penrose and P. C. Fife, *Physica D* **43**, 44 (1990).
 - [5] S-L. Wang, R. F. Sekerka, A. A. Wheeler, B. T. Murray, S. R. Coriell, R. J. Braun, and G. B. McFadden, *Physica D* **69**, 189 (1993).
 - [6] A. A. Wheeler, W. J. Boettinger, and G. B. McFadden, *Phys. Rev. A* **45**, 7424 (1992); *Phys. Rev. E* **47**, 1893 (1993).
 - [7] G. Caginalp and W. Xie, *Phys. Rev. E* **48**, 1897 (1993).
 - [8] J. A. Warren and W. J. Boettinger, *Acta Metall. Mater.* **43**, 689 (1995).
 - [9] A. Karma, *Phys. Rev. E* **49**, 2245 (1994).
 - [10] K. R. Elder, F. Drolet, J. M. Kosterlitz, and M. Grant, *Phys. Rev. Lett.* **72**, 677 (1994).
 - [11] A. A. Wheeler, G. B. McFadden, and W. J. Boettinger, *Proc. R. Soc. London, Ser. A* **452**, 495 (1996).
 - [12] R. Kobayashi, *Physica D* **63**, 410 (1993).
 - [13] R. Kobayashi, *Exp. Math.* **3**, 60 (1994).
 - [14] A. A. Wheeler, B. T. Murray, and R. Schaefer, *Physica D* **66**, 243 (1993).
 - [15] R. Kupferman, O. Shochet, and E. Ben-Jacob, *Phys. Rev. E* **50**, 1005 (1994).

- [16] B. T. Murray, A. A. Wheeler, and M. E. Glicksman, *J. Cryst. Growth* **47**, 386 (1995).
- [17] S-L. Wang and R. F. Sekerka, *Phys. Rev. E* **53**, 3760 (1996).
- [18] G. B. McFadden, A. A. Wheeler, R. J. Braun, S. R. Coriell, and R. F. Sekerka, *Phys. Rev. E* **48**, 2016 (1993).
- [19] A. Karma and W. J. Rappel, *Phys. Rev. E* **53**, R3017 (1996).
- [20] A. Karma and W. J. Rappel, in *Mathematics of Microstructural Evolution*, edited by Long-Qing Chen *et al.* (The Minerals, Metals, and Materials Society and the Society for Industrial and Applied Mathematics, 1996), p. 195.
- [21] A. Karma and W. J. Rappel, *Phys. Rev. Lett.* **77**, 4050 (1996).
- [22] T. Abel, E. Brener, and H. Müller-Krumbhaar, *Phys. Rev. E* **55**, 7789 (1997).
- [23] A. Bösch, H. Müller-Krumbhaar, and O. Shochet, *Z. Phys. B* **97**, 367 (1995).
- [24] J. A. Sethian and J. Strain, *J. Comput. Phys.* **98**, 2313 (1992).
- [25] R. Almgren, *J. Comput. Phys.* **106**, 337 (1993).
- [26] A. R. Roosen and J. E. Taylor, *J. Comput. Phys.* **114**, 113 (1994).
- [27] T. Ihle and H. Müller-Krumbhaar, *Phys. Rev. E* **49**, 2972 (1994).
- [28] V. L. Ginzburg and L. D. Landau, *Zh. Éksp. Teor. Fiz.* **20**, 1064 (1950) [*Sov. Phys. JETP* **20**, 1064 (1950)].
- [29] J. W. Cahn and J. E. Hilliard, *J. Chem. Phys.* **28**, 258 (1958).
- [30] B. I. Halperin, P. C. Hohenberg, and S-K. Ma, *Phys. Rev. B* **10**, 139 (1974).
- [31] J. S. Langer (unpublished).
- [32] G. Caginalp, *Phys. Rev. A* **39**, 5887 (1989).
- [33] R. J. Braun and M. T. Murray, *J. Cryst. Growth* **174**, 41 (1997).
- [34] A. Schmidt, *J. Comput. Phys.* **125**, 293 (1996).
- [35] R. Almgren and A. S. Almgren, in *Mathematics of Microstructural Evolution*, edited by L-Q. Chen *et al.* (The Minerals, Metals and Materials Society and the Society of Industrial and Applied Mathematics, 1996), p. 205.
- [36] P. C. Fife and O. Penrose, *Electron. J. Diff. Eq.* **1**, 1–49 (1995).
- [37] D. A. Kessler and H. Levine, *Phys. Rev. B* **33**, 7687 (1986).
- [38] D. I. Meiron, *Phys. Rev. A* **33**, 2704 (1986).
- [39] M. Ben Amar and B. Moussallam, *Physica D* **25**, 155 (1987).
- [40] M.-A. Lemieux, J. Liu, and G. Kotliar, *Phys. Rev. A* **36**, 1849 (1987).
- [41] E. A. Brener and V. I. Mel'nikov, *Adv. Phys.* **40**, 53 (1991).
- [42] A. Karma and W.-J. Rappel, *J. Cryst. Growth* **174**, 54 (1997).
- [43] J. S. Langer, *Rev. Mod. Phys.* **52**, 1 (1980).
- [44] J. S. Langer, in *Chance and Matter*, Lectures on the Theory of Pattern Formation, Les Houches, Session XLVI, edited by J. Souletie, J. Vannimenus, and R. Stora (North-Holland, Amsterdam, 1987), pp. 629–711.
- [45] D. Kessler, J. Koplik, and H. Levine, *Adv. Phys.* **37**, 255 (1988).
- [46] D. A. Kessler, J. Koplik, and H. Levine, *Phys. Rev. A* **31**, 1712 (1985).
- [47] E. Ben-Jacob, N. D. Goldenfeld, B. G. Kotliar, and J. S. Langer, *Phys. Rev. Lett.* **53**, 2110 (1984).
- [48] J. S. Langer, *Phys. Rev. A* **33**, 435 (1986).
- [49] D. A. Kessler and H. Levine, *Acta Metall.* **36**, 2693 (1988).
- [50] A. Barbieri and J. S. Langer, *Phys. Rev. A* **39**, 5314 (1989).
- [51] M. Ben Amar and E. Brener, *Phys. Rev. Lett.* **71**, 589 (1993).
- [52] E. Brener, *Phys. Rev. Lett.* **71**, 3653 (1993).
- [53] S-C. Huang and M. E. Glicksman, *Acta Metall.* **29**, 701 (1981).
- [54] M. E. Glicksman and N. B. Singh, *J. Cryst. Growth* **98**, 277 (1989).
- [55] E. R. Rubinstein and M. E. Glicksman, *J. Cryst. Growth* **112**, 84 (1991).
- [56] M. Muschol, D. Liu, and H. Z. Cummins, *Phys. Rev. A* **46**, 1038 (1992).
- [57] M. E. Glicksman, M. B. Koss, A. Lupulescu, L. A. Tennenhouse, and J. C. LaCombe (unpublished).
- [58] G. Caginalp and X. Chen, in *On the Evolution of Phase Boundaries*, edited by M. E. Gurtin and G. B. McFadden, The IMA Volumes in Mathematics and Its Applications Vol. 43 (Springer-Verlag, New York, 1992), p. 1.
- [59] A. A. Wheeler and G. B. McFadden, *Europ. J. Appl. Math.* **7**, 367 (1996).
- [60] J. W. Cahn and D. W. Hoffman, *Acta Metall.* **22**, 1205 (1974).
- [61] R. J. Braun, G. B. McFadden, and S. R. Coriell, *Phys. Rev. E* **49**, 4336 (1994), and references therein.
- [62] W. H. Press, S. A. Teukolsky, W. T. Vetterling, and B. P. Flannery, *Numerical Recipes* (Cambridge University Press, Cambridge, England, 1992).
- [63] G. E. Nash and M. E. Glicksman, *Acta Metall.* **22**, 1283 (1974).
- [64] J. W. Cahn, *Acta Metall.* **8**, 554 (1960).
- [65] D. A. Kessler, H. Levine, and W. N. Reynolds, *Phys. Rev. A* **42**, 6125 (1990).
- [66] P. W. Voorhees, S. R. Coriell, G. B. McFadden, and R. F. Sekerka, *J. Cryst. Growth* **67**, 425 (1984).
- [67] A. Karma (unpublished).
- [68] G. P. Ivantsov, *Dokl. Akad. Nauk SSSR* **58**, 567 (1947).
- [69] M. Ben Amar and E. Brener, *Phys. Rev. Lett.* **75**, 561 (1995).
- [70] M. Ben Amar, *Phys. Rev. A* **41**, 2080 (1990).
- [71] A. Dougherty, P. D. Kaplan, and J. P. Gollub, *Phys. Rev. Lett.* **58**, 1652 (1987).
- [72] E. Brener and V. I. Melnikov, *JETP* **80**, 341 (1995).
- [73] J. Maurer, B. Perrin, and P. Tabeling, *Europhys. Lett.* **14**, 575 (1991).
- [74] J. C. LaCombe, M. B. Koss, V. E. Fradkov, and M. E. Glicksman, *Phys. Rev. E* **52**, 2778 (1995).
- [75] R. Almgren, W. S. Dai, and V. Hakim, *Phys. Rev. Lett.* **71**, 3461 (1993).